ELEMENTA
Science of the Anthropocene

Svensson, G, et al. 2023. Warm air intrusions reaching the MOSAiC expedition in April 2020—The YOPP targeted observing period (TOP). *Elem Sci Anth*, 11: 1.
DOI: https://doi.org/10.1525/elementa.2023.00016

RESEARCH ARTICLE

Warm air intrusions reaching the MOSAiC expedition in April 2020—The YOPP targeted observing period (TOP)

Gunilla Svensson[1,2,*], Sonja Murto[1], Matthew D. Shupe[3], Felix Pithan[4], Linus Magnusson[5], Jonathan J. Day[5], James D. Doyle[6], Ian A. Renfrew[7], Thomas Spengler[8], and Timo Vihma[9]

In the spring period of the Multidisciplinary drifting Observatory for the Study of Arctic Climate (MOSAiC) expedition, an initiative was in place to increase the radiosounding frequency during warm air intrusions in the Atlantic Arctic sector. Two episodes with increased surface temperatures were captured during April 12–22, 2020, during a targeted observing period (TOP). The large-scale circulation efficiently guided the pulses of warm air into the Arctic and the observed surface temperature increased from −30°C to near melting conditions marking the transition to spring, as the temperatures did not return to values below −20°C. Back-trajectory analysis identifies 3 pathways for the transport. For the first temperature maximum, the circulation guided the airmass over the Atlantic to the northern Norwegian coast and then to the MOSAiC site. The second pathway was from the south, and it passed over the Greenland ice sheet and arrived at the observational site as a warm but dry airmass due to precipitation on the windward side. The third pathway was along the Greenland coast and the arriving airmass was both warm and moist. The back trajectories originating from pressure levels between 700 and 900 hPa line up vertically, which is somewhat surprising in this dynamically active environment. The processes acting along the trajectory originating from 800 hPa at the MOSAIC site are analyzed. Vertical profiles and surface energy exchange are presented to depict the airmass transformation based on ERA5 reanalysis fields. The TOP could be used for model evaluation and Lagrangian model studies to improve the representation of the small-scale physical processes that are important for airmass transformation. A comparison between MOSAiC observations and ERA5 reanalysis demonstrates challenges in the representation of small-scale processes, such as turbulence and the contributions to various terms of the surface energy budget, that are often misrepresented in numerical weather prediction and climate models.

Keywords: Arctic climate, Warm air intrusions, MOSAiC, Lagrangian airmass transformation, Reanalysis evaluation

1. Introduction

The Arctic is a region with a net deficit of energy at the top of the atmosphere. This loss of energy must be balanced with heat import from lower latitudes for a climate in balance and the transport is both in terms of sensible and latent heat (Bengtsson et al., 2011). The atmospheric transport into the Arctic is partly due to the mean flow, but above all due to transient eddies, that is, the synoptic scale dynamical systems that populate the midlatitudes and extend into the Arctic. These transient features are often referred to as warm and/or moist air intrusions. It has been shown that the strongest moisture intrusions at 70°N, defined as exceeding 200 Tg day^{-1} deg^{-1} for at least 1.5 consecutive days in a sector of at least 9° zonal extent during 1999–2010, on average 14 per season, account for about one third of the moisture transport into the Arctic (Woods et al., 2013). These types of events substantially affect the local surface energy budget, temperature, and moisture (e.g., Messori et al., 2018; Fearon et al., 2021; Murto et al., 2022).

---

[1] Department of Meteorology and Bolin Centre for Climate Research, Stockholm University, Stockholm, Sweden

[2] Department of Engineering Mechanics, KTH Royal Institute of Technology, Stockholm, Sweden

[3] Cooperative Institute for Research in Environmental Sciences, University of Colorado and Physical Sciences Laboratory, National Oceanic and Atmospheric Administration, Boulder, CO, USA

[4] Alfred Wegener Institute, Helmholtz Centre for Polar and Marine Research (AWI), Bremerhaven/Potsdam, Germany

[5] European Centre for Medium-Range Weather Forecasts, Reading, UK

[6] U.S. Naval Research Laboratory, Marine Meteorology Division, Monterey, CA, USA

[7] School of Environmental Sciences, University of East Anglia, Norwich, UK

[8] Geophysical Institute, University of Bergen and Bjerknes Centre for Climate Research, Bergen, Norway

[9] Meteorological Research, Finnish Meteorological Institute, Helsinki, Finland

[*] Corresponding author:
Email: gunilla@misu.su.se

The Arctic is also a region subject to rapid climate change with an amplification of regional temperature change that during the latest decades has been almost 4 times the global value, a signal that is not captured by the state-of-the-art climate models (Rantanen et al., 2022). Changes in the net atmospheric energy transport are suggested as one of the mechanisms that give rise to Arctic amplification, in addition to changes in ocean transport and several feedback mechanisms that operate in the region (e.g., Pithan and Mauritsen, 2014; Goosse et al., 2018).

Most studies of Arctic climate and climate change are performed using reanalysis and/or climate models. Although reanalyses blend observations with a model representation of the climate system, the sparse observations and poorly represented physical processes over the polar regions can limit their quality (Dufour et al., 2016; Graham et al., 2019a; Naakka et al., 2019; Renfrew et al., 2021). Boundary-layer processes and turbulent surface fluxes, clouds, and radiation are uncertain fields in reanalyses (e.g., Graham et al., 2019a) and in climate models (e.g., Svensson and Karlsson, 2011). It is also clear that these small scale parameterized processes are important for the skill of weather forecasts (e.g., Jung et al., 2016; Tjernström et al., 2021) and are also important for how Arctic climate change evolves in climate models (Pithan and Mauritsen, 2014).

To properly evaluate and possibly improve the quality of process representation in reanalyses and models, more in situ observations are needed. This is especially the case in the high Arctic during winter, as the region is more accessible during summer (e.g., Tjernström et al., 2014). The recent yearlong Multidisciplinary drifting Observatory for the Study of Arctic Climate (MOSAiC) expedition (Shupe et al., 2022), that started in September 2019, provided unique observations along a drifting path of sea ice across the Central Arctic. It was based on the German research icebreaker Polarstern (Knust, 2017) with additional observations on the adjacent sea ice and in a distributed network extending about 40 km in all directions.

Recognizing the importance of warm air intrusions and their potential impacts on sea ice melt onset (e.g., Mortin et al., 2016), the WMO World Weather Research Program (WWRP) Polar Prediction Project (PPP; Jung et al., 2015) organized enhanced observational activities during spring 2020. This so-called targeted observing period (TOP) successfully captured a series of warm air intrusion events in mid-April, which marked the transition from the cold winter toward the relatively warmer spring, and included 2 brief periods when the surface approached the melting point (Shupe et al., 2022). The warm air intrusions also brought unusual amounts of aerosols to the central Arctic (Dada et al., 2022). Due to these events, the monthly mean MOSAiC-trajectory temperature was among the warmest 12 Aprils in the 1979–2020 ERA5 record (Rinke et al., 2021). The daily-averaged temperature and integrated moisture content on April 16 and 19 were record-breaking compared to the reanalysis record; however, this might be a biased result as there were no observations to assimilate in this region during the other years.

Here, we present the TOP organization that was put in place to capture the intrusion events and the additional observations that are available. The TOP period is defined as April 12–22, 2020, during which 2 episodes of warm air intrusions are identified. The European Centre for Medium-range Weather Forecasts (ECMWF) ERA5 reanalysis (Hersbach et al., 2020) provides an overview of the synoptic situation leading up to the warm air events as well as the evolution during and after. Back trajectories are used to examine the Lagrangian evolution of the airmasses that reach the MOSAiC site. The evaluation of the ERA5 at the MOSAiC site during the 10-day period in April is also presented.

2. TOP planning and engagement of the met services

The WWRP PPP objective is to "promote cooperative international research enabling development of improved weather and environmental prediction services for the polar regions, on time scales from hours to seasonal" (Jung et al., 2015). As a complementary MOSAiC activity, a PPP task team organized support from national Met Services (**Table 1**) to be on stand-by to release extra radiosondes at their regular stations in the case of an interesting situation. While prior special observing periods organized by the PPP (Day et al., 2019) were used to conduct observing system experiments, the TOP was specifically designed to examine the vertical structure of latitudinal advection events and specifically the Lagrangian airmass evolution as suggested by Pithan et al. (2018). The location of the main MOSAiC observatory was at this time in the Atlantic sector of the Arctic Ocean (**Figure 1a**) and the targeted sounding stations are located around the Nordic Seas (**Figure 1b**).

A communication procedure was set up that alerted the launching stations 5 days ahead of a forecast warm air intrusion event with a request for start and end dates for additional soundings. An update followed 48 h ahead of the event followed by a confirmation 24 h before. Daily email updates were sent until the end of the TOP. The procedure was put in place in early March 2020.

Tailored forecast products, including trajectories, from the ECMWF and the German Weather Service (DWD) were used to carefully assess the synoptic evolution allowing interesting meteorological situations to be identified. Especially valuable products were the ECMWF polar view Extreme Forecast Index (Lalaurette, 2003) of water vapor transport and forecast back trajectories from the position of Polarstern using the Lagrangian analysis tool (LAGRANTO; Sprenger and Wernli, 2015). The 10-day TOP started on April 12 with extra soundings available from April 14. During spring 2020, the Covid-19 pandemic resulted in a large loss of aircraft reports (c.f. AMDAR program, Petersen, 2016), with an approximately 75% decrease during the second half of April (Ingleby et al., 2021). Many of the Met Services increased their sounding frequency to make up for this deficiency (see **Table 1**). Thus, in addition to the TOP enhancement, more soundings than usual were launched in the region to prevent forecast degradation. However, the forecast quality (and thus likely reanalysis quality) was not affected as much as anticipated (Ingleby et al., 2021).

Unfortunately, 2 of the stations that agreed to participate in the YOPP TOP had technical problems; the Swedish

Table 1. Sounding stations, location, and available times, including the extra TOP requested ones and from 2 research stations (COMBLE and Greenland Summit), during the period April 12–21

Name/ Operated by	Latitude/ Longitude	12 April	13 April	14 April	15 April	16 April	17 April	18 April	19 April	20 April	21 April	Comment
Eureka/	80.08/	00 12	00 12	00 12	00 12	00 12	00 12	00 12	00 12	00 12	00 12	Regular
ECCC	−86.42											
Keflavik/	63.99/	00 12	00 12	00 12	00 12	00 12	00 12	00 12	00 12	00 12	00 12	Regular
IMO	−22.59							06 18				TOP
Egilsstadir/	65.28/											Regular
IMO	−14.40						06	00 06				TOP
		12	12	12		12	12	12	12	12		AMDAR
Sodankylä/	67.37/	00 12	00 12	00 12	00 12	00 12	00 12	00 12	00 12	00 12	00 12	Regular
FMI	26.63	06 18	06 18	06 18	06 18	06 18	06 18	06 18	06 18	06 18	06 18	TOP
Ny Ålesund/	78.92/	12	12	12	12	12	12	12	12	12	12	Regular
AWI	11.92			00 06 18	00				00 06 18			TOP
Tasiilaq/	65.61/	00 12	00 12	00 12	00 12	00 12	00 12	00 12	00 12	00 12	00 12	Regular
DMI	−37.64						06 18	06				TOP
Polarstern/		00 06	00 06	00 06	00 06	00 06	00 06	00 06	00 06	00 06	00 06	Regular
AWI		12 18	12 18	12 18	12 18	12 18	12 18	12 18	12 18	12 18	12 18	
				09 15 21	09 15 21	09 15 21	09 15 21	09 15 21	09 15 21	09 15		TOP
Bear Island/	74.15/	00 06	00 06	00 06	00 06	00 06	00 06	00 06	00 06	00 06	00 06	Regular
MetNo	19.00	12 18	12 18	12 18	12 18	12 18	12 18	12 18	12 18	12 18	12 18	
Jan Mayern/	70.94/	00 06	00 06	00 06	00 06	00 06	00 06	00 06	00 06	00 06	00 06	Regular
MetNo	−8.67	12 18	12 18	12 18	12 18	12 18	12 18	12 18	12 18	12 18	12 18	
Andoya/	69.32/	00 12	–	–	–	Technical	–	–	–	–	12	Regular
MetNo	16.13					issues						
COMBLE/	69.14/	00 06	00 06	00 06	00 06	00 06	00 06	00 06	00 06	00 06	00 06	
research	15.68	12 18	12 18	12 18	12 18	12 18	12 18	12 18	12 18	12 18	12 18	
Summit/	72.60/	00 12	00 12	00 12	00 12	00 12	00 12		12	00 12	00 12	
NSF	−38.42											

TOP = targeted observing period; COMBLE = Cold-Air Outbreaks in the Marine Boundary Layer Experiment; ECCC = Environment and Climate Change Canada; IMO = Icelandic Meteorological Office; FMI = Finnish Meteorological Institute; AWI = Alfred Wegener Institute; DMI = Danish Meteorological Institute; MetNo = MetNorway.

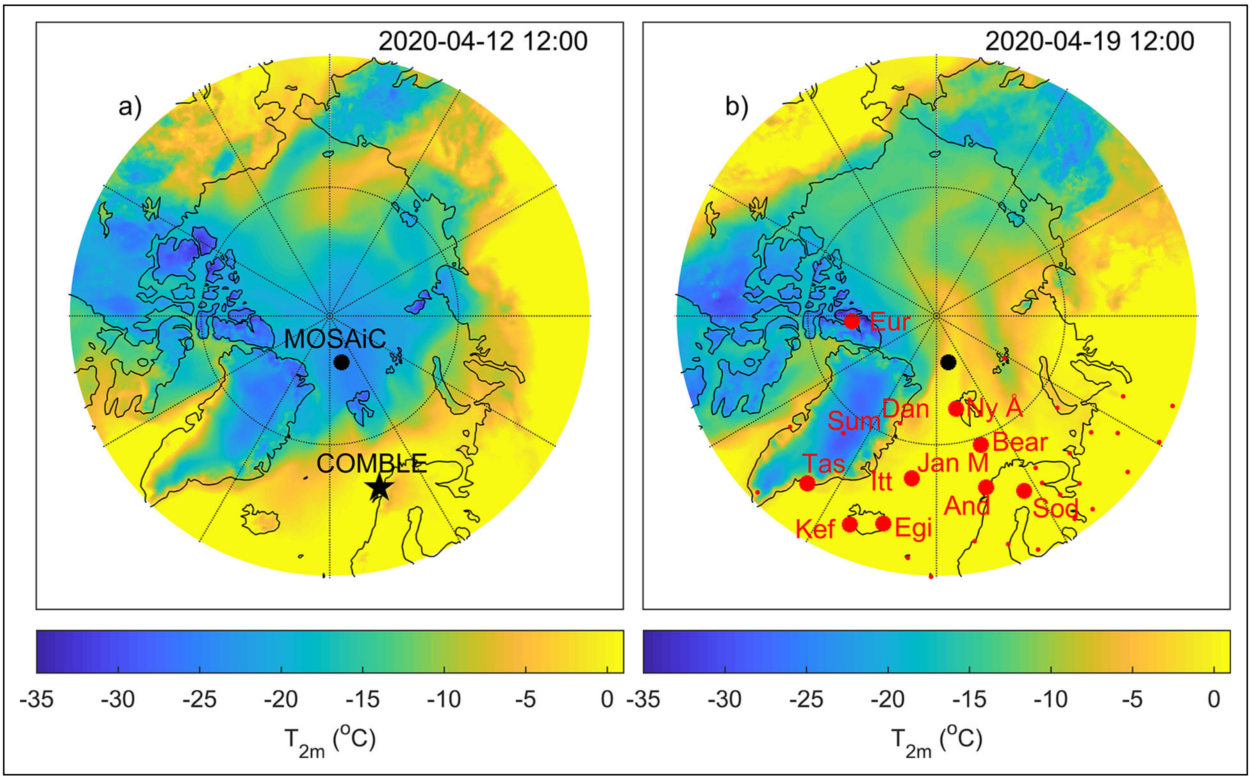

Figure 1. Near surface temperature in °C at noon UTC (a) in the beginning (April 12, 2020) and (b) end of the TOP (April 19, 2020) based on ERA5 data. Also shown are the main location of the sounding stations at the Multidisciplinary drifting Observatory for the Study of Arctic Climate (black filled circle) and Cold-Air Outbreaks in the Marine Boundary Layer Experiment (black star) sites and also in (b) available sounding stations in the Atlantic Sector (red markers). The sounding stations that were engaged for extra launches (see **Table 1**) are shown with a larger marker.

Meteorological and Hydrological Institute station in Luleå (no soundings) and the Met Norway station at Andenes (no soundings 12 UTC April 12 to noon UTC April 21). Fortunately, Cold-Air Outbreaks in the Marine Boundary Layer Experiment (COMBLE; Geerts et al., 2022) operated a sounding station at Andenes, not far from the operational station, providing soundings that are included here as well (see **Table 1**). In addition, regular soundings in the Atlantic sector from approximately the middle of Greenland to part of Russia, retrieved from the ECMWF archive, are also useful for Lagrangian analysis (see **Figure 1b**).

In total, the TOP added more than 50 radiosoundings during the 10-day period (**Table 1**). These additional soundings, when combined with the detailed observations made in northern Norway as part of COMBLE (Geerts et al., 2022) and over the sea ice as part of MOSAiC (Shupe et al., 2022), provide a comprehensive observational data set to examine 2 mid-April episodes of warm air intrusions and to assess their representation by models.

3. Observations, trajectories, and reanalysis data

During the TOP period, many radiosondes were launched at key locations, including the extra profiles obtained specifically in support of the TOP (e.g., **Table 1**). While all of the radiosoundings (except those from COMBLE) were uploaded to the Global Telecommunications System and thereby aided modeling and reanalysis products, some of these observations were used directly in this study. Specifically, profiles measured at the following fixed land stations are used here: Bear Island (Bear), Andøya (And), Ny Ålesund (Ny Å), Summit Station (Sum), Tasiilaq (Tas), Ittoqqortoormiit (Itt), and Keflavik (Kef) (see **Figure 1b**). Complementing these radiosoundings, there were also additional radiosondes launched from the Polarstern at the drifting MOSAiC site. While the standard operations at MOSAiC entailed 4 radiosoundings per day, during the period spanning April 14 through the middle of April 20, the radiosounding frequency was increased to 7 per day. A profile was obtained every 3 h, except for one 6-h period without soundings in the middle of the night.

Supporting the expanded radiosonde observations, an extensive collection of ground-based observations was also made at the MOSAiC site, some of which are used in the analysis conducted here. On the sea ice within about 400 m of Polarstern was the “Met City” installation, which included a 10-m meteorological tower that measured near-surface pressure, temperature, humidity, and winds at multiple levels, in addition to instrumentation for deriving surface turbulent sensible and latent heat fluxes (Cox et al., 2021; Cox et al., n.d.). Near the tower was a suite of upward- and downward-looking radiometers measuring surface broadband shortwave and longwave radiative fluxes (Riihimaki, 2019). Onboard Polarstern was a suite of instruments including a cloud radar, depolarization lidar, microwave radiometers, and a ceilometer that were collectively used to derive a cloud phase and microphysical properties (Shupe et al., 2015; Shupe, 2022). More information on all of the MOSAiC atmospheric observations can be found in Shupe et al. (2022).

ERA5 fields (Hersbach et al., 2020) are extensively used here to explore the spatial and temporal evolution in the region, despite the limitations that reanalysis may have in the Arctic (see Section 5). ERA5, or its predecessor ERA-Interim, has been shown to accurately reproduce the wind, temperature, and humidity fields in the Arctic (Graham et al., 2019b). A number of surface and model level fields were obtained that were used in the trajectory calculations and for further analysis along the trajectories. An evaluation of the closest ERA5 grid point to the observations at the MOSAiC main observatory was performed.

Four-day backward trajectories were computed using the LAGRANTO tool (Sprenger and Wernli, 2015), initialized at the MOSAiC site every hour within the TOP at 700-, 800-, 850-, and 900-hPa pressure levels. Backward trajectories were computed using ERA5 data with hourly temporal resolution and a spatial resolution of 1°. Additionally, 1 forward trajectory was initialized at 800 hPa.

Large-scale circulation patterns associated with the identified warm air intrusions during the TOP are explored using cyclone tracks and diagnosis of atmospheric blocks. Cyclone tracks, computed hourly with a spatial resolution of 0.25°, were identified with an SLP-based algorithm (Jakob Beran, personal communication, 05/10/2022). Blocks were identified using a potential vorticity (PV) method following Schwierz et al. (2004) and Croci-Maspoli et al. (2007) that is based on negative, vertically averaged upper-level (150–500 hPa) PV anomalies (below -1.3 pvu) persisting for at least 5 days. For the detection of blocks, hourly data on model levels were interpolated to a 0.5° grid.

4. Large-scale setting

The large-scale circulation during the TOP (**Figure 2**) and accompanying meridional transport results in 2 periods of near-surface temperature being close to the melting point and relative humidity (with respect to water) close to 100% at the MOSAiC site. These are centered on April 16 and 19 (**Figure 3**) and are here referred to as 2 episodes with 3 events (see Sections 6.1–6.3, all time references are in UTC). The events are defined as the start times of the backtrajectories (vertical dashed lines in **Figure 3**). The warm airmasses are guided by the large-scale circulation and arrive at the MOSAiC location on April 14 when the steady increase in the near surface temperature commences. At the end of the TOP, a substantially warmer central Arctic is evident (compare **Figure 1a** and **b**).

Despite the variable large-scale setting during the TOP, trajectories arriving at the Polarstern at pressure levels between 700 and 900 hPa align vertically around 1 day before arrival during intense warm air advection (**Figure 2a**, **g**, and **j**), thus indicating a vertically coherent flow for the last 24 h before arriving at the observational site. We study trajectories initiated at 12 UTC on April 16 and at 00 and 12 UTC on April 19 (dashed vertical lines in **Figure 3**) that capture the pathways of the airmasses contributing to the warm episodes.

On April 12 at 12 UTC, 4 days prior to the first temperature maximum at the MOSAiC site (**Figure 3**), 2 narrow bands of moist air that reach 70°N are associated with low-pressure centers west of Greenland and over Scandinavia (Figure S1a in the Supplemental Materials). These bands move eastward guided by the high-pressure ridges and related blocks located over the North Atlantic northwest of the United Kingdom (UK) and over the Urals 1 day later (Figure S1c). The backward trajectory initialized at 900 hPa is located south of Greenland on April 12 (green in **Figure 2a**). The air is transported zonally following the advection corridor created by the pressure dipole across the North Atlantic and slightly descends from the influence of the blocking to the east of the trajectory during the first days of its journey (Figure S1d).

Trajectories ending at higher altitudes at the MOSAiC site (orange and blue in **Figure 2a**) are located around 1,000 hPa (not shown) west of Scandinavia 2–3 days prior to arrival. On April 14, 12 UTC, the Ural blocking strengthens and a cyclone associated with the eastward moving low-pressure center is detected between Greenland and Svalbard (not shown). From the influence of the large-scale circulation patterns, all trajectories are deflected northwards; after passing the Andøya station less than 2 days prior to arrival, the 2 trajectories ascend from the surface up to 700 and 800 hPa, passing the Bear Island station and finally arrive at the MOSAiC site. The trajectory initialized at 900 hPa stays at the same level for the last 2 days, vertically aligned with the 2 others during the day prior to arrival. On April 16, 12 UTC, the narrow band of moist air that a few days prior extended to Scandinavia now reaches into the high Arctic, guided by a cyclone west of Polarstern (**Figure 2b**) and the Ural blocking (**Figure 2a**), bringing warmer and moister air to the MOSAiC site. This further favors the formation of liquid clouds (**Figure 2c**), causing a strong cloud surface radiative effect (not shown).

The synoptic situation 1 day later, on April 17, 12 UTC (**Figure 2d–f**), is similar to the previous day, however with the moist air intrusion deflected westward following the cyclone moving across the Arctic and the blocking to the east (Figure S2). In comparison to the previous day, trajectories recirculate cyclonically in the Arctic once they pass Ny-Ålesund and drift over the sea ice. Along these trajectories, the airmasses are subjected to radiative cooling and drying during the 3 days prior to arrival at the MOSAiC site. The air at Polarstern on April 17 is dry (**Figure 2e**) without liquid clouds (**Figure 2f**) and the skin temperature drops temporarily below −15°C (**Figure 3**).

The 2 following events during the second warm episode are only 12 h apart. They are affected by different synoptic systems and thus have different airmass pathways (**Figure 2g–l**). In comparison to the first warm episode, these air parcels take a more meridional pathway following a warm airmass intrusion that reaches the MOSAiC site after crossing the North Atlantic and passing west of Svalbard. Four days prior to the second event (April 19, 00 UTC), trajectories initialized from higher

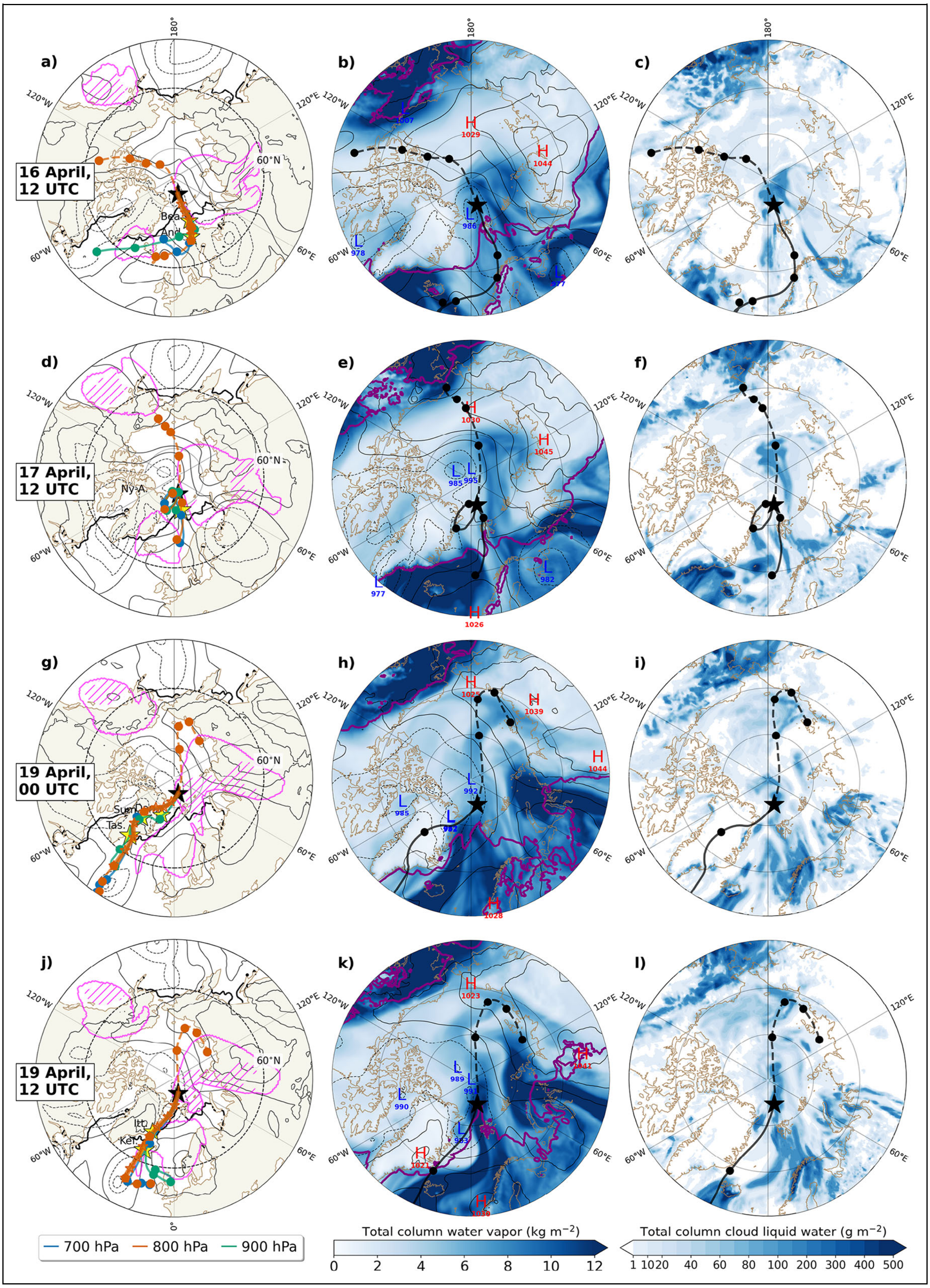

Figure 2. Large scale setting on (a–c) April 16, 12 UTC, (d–f) April 17, 12 UTC, (g–i) April 19, 00 UTC, and (j–l) April 19, 12 UTC along with trajectories initiated at MOSAiC (star) at 700 (blue), 800 (orange and black in middle and right columns), and 900 (green) hPa with dots every 24 h and stars every 6 h (left column). Atmospheric blocking (pink contour; hatched when blocked for 4 days), sea level pressure (SLP) (hPa, black contours every 10 hPa; solid for SLP > 1,000 hPa) and sea-ice edge (sea ice concentration of 0.15; black thick line). Yellow stars indicate sounding stations if located within 50-km distance from a trajectory. Middle panel shows total column water vapor (kg m^{-2}), 0°C at 2 m (purple solid) and SLP contours. Right column shows total column cloud liquid water (g m^{-2}). Note the larger geographical area in left column.

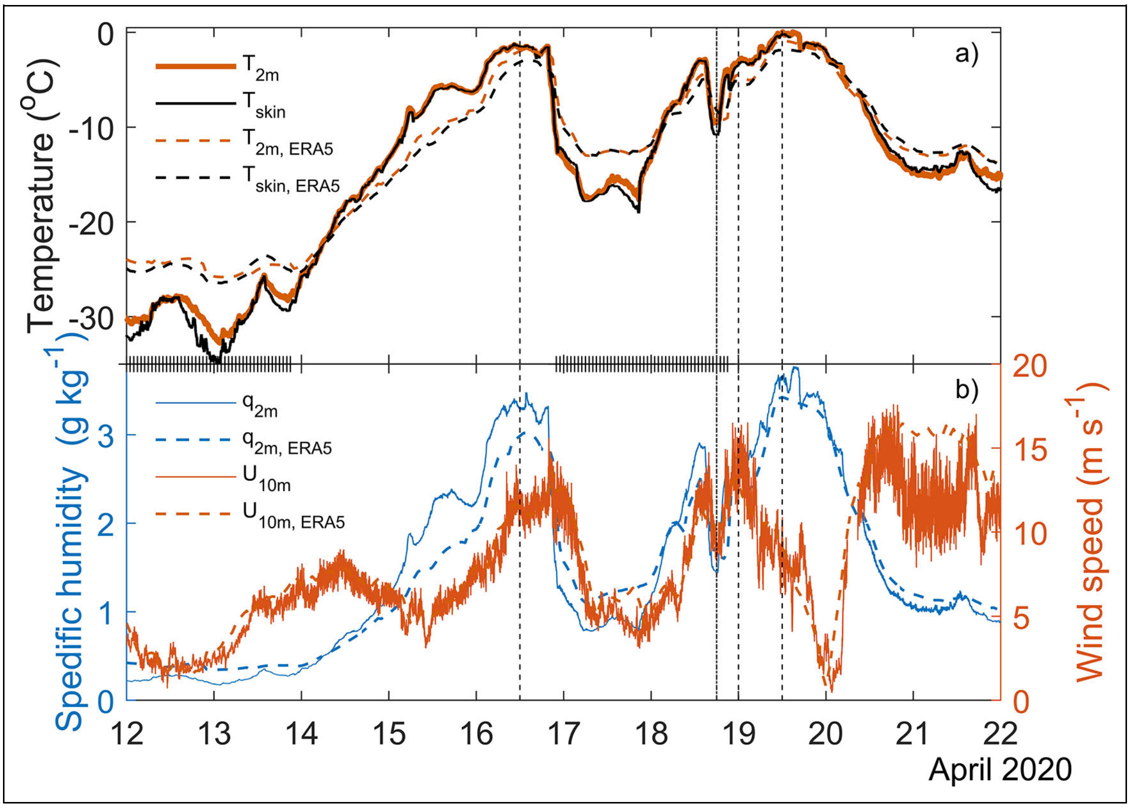

Figure 3. Observed (solid lines) and reanalysis (dashed lines) near surface (at 2 m height) and skin temperatures (°C, a), near surface specific humidity (g kg^{-1}, left axis in b) and wind speed at 10-m height (m s^{-1}, right axis in b) during the TOP (targeted observing period, April 12–22, 2020) at the MOSAiC site. Vertical dashed lines show the arrival times for the trajectories discussed in Sections 6.1–6.3, and the dashed-dotted line is the arrival time for the trajectories discussed in Section 6.4. Sea ice cover of unity in the reanalysis is marked with symbols along the time axes in (a).

pressure levels are located over the warm and moist North Atlantic (**Figure 2g**). Air then moves northward, while descending toward the surface (not shown) under the influence of the blocking located over the UK (Figure S3a, with similar position as in **Figure 2a**). Two cyclones, originating northeast of North America, are related to the low-pressure area over and west of Greenland that helps guide the air parcels northward and the air parcels are further steered by the blocks to the east.

On April 16 at 12 UTC, less than 3 days prior to arrival, the pressure dipole across southern Greenland drives the air parcels toward Greenland (Figure S3d similar to the situation in **Figure 2a**). The air parcel initialized at 900 hPa reaches Tasiilaq station shortly after, ascends over Greenland, and passes Summit station 2 days prior to arrival, whereafter it descends east of Greenland and passes Danmarkshavn station 1 day later (**Figure 2g**). The 2 lower pressure trajectories reach the south of Greenland 36 h before arrival, cross over the terrain and descend following a more northerly pathway compared to the trajectory closer to the surface.

The final warm event occurs half a day later, on April 19, 12 UTC (**Figure 2j–l**). Keeping almost the same pressure during their whole journey, these air parcels take a more easterly pathway, thus not crossing over Greenland but instead following the coast before reaching the MOSAiC site on April 19, 12 UTC (**Figure 2j** and Figure S4). These trajectories are less influenced by the North-Atlantic cyclones (not shown), rather they are guided by the blocking over the UK that moves northeast and merges with the Ural blocking on April 18, 12 UTC (Figure S4g; similar to the synoptic situation shown in **Figure 2g**). This large-scale setting creates a clear meridional pathway for the warm and moist airmass to reach deep into the Arctic. These air parcels travel across the North Atlantic for several days, pass the Keflavik station, and finally reach the ice edge 24 h before arrival at Polarstern. The air parcel initialized at 800 hPa takes a small detour over the Ittoqqortoormiit station on Greenland before aligning with the other 2 trajectories (**Figure 2j**). A cyclone forms at the MOSAiC site less than 12 h before the final warm event (not shown), helping the moist and warm air to reach the MOSAiC site, again favoring liquid cloud formation (**Figure 2k** and **l**).

5. MOSAiC observations and evaluation of ERA5

5.1. Near surface conditions

At the beginning of the TOP, the observed near surface and skin temperatures at the MOSAiC site were around −30°C with a diurnal cycle of 5°–8° (**Figure 3a**). At midnight going into April 14, the temperature starts to increase, and at midday on April 16, the first maximum

Table 2. MOSAiC observations; for more information, see Shupe et al. (2022)

Instrument	Measurement	Reference
ICERAD: radiometers, rapid gas sampler, and meteorology package	Up- and downwelling broadband longwave and shortwave surface radiation	Riihimaki (2019)
10-m tower: sonic anemometer	Temperature, winds, humidity, sensible, and latent heat flux	Cox et al. (2021)
Combined: Ka-band ARM Zenith Radar, microwave radiometers, micropulse lidar, ceilometer, and radiosonde	Cloud liquid and ice water paths derived from multiple measurements and a cloud classification algorithm	Shupe (2022)

MOSAiC = Multidisciplinary drifting Observatory for the Study of Arctic Climate.

is reached with the skin temperature close to the melting point for the snow-covered surface. The specific humidity follows the shape of the temporal evolution of the temperature. There is an abrupt drop in both variables late on April 16 down to almost -20°C and about 1 g kg^{-1} in specific humidity (RH drops to 80% from near 100%, not shown). On April 18, the temperature increases again, however, the specific humidity does not reach as high as on April 16, and after a short dip in both at 18 UTC April 18, the RH reaches almost 100% (not shown) and the skin and surface air temperatures almost reach the melting point 18 h later.

After the arrival of these episodes of warmer and moister air, the temperature drops but only to about -15°C, thus 15° warmer than at the beginning of the TOP. The temperature does not go much below -15°C for the rest of the spring; thus, this period marks a transition from winter to spring conditions (Shupe et al., 2022). The wind speed does not covary with the temperature; rather, the wind speed maxima (reaching over 10 m s^{-1}) tends to lag the temperature maxima by 12–24 h (**Figure 3b**). It is interesting to see how well ERA5 captures the wind speed (and direction, not shown), except for the last 1.5 days when the reanalysis overestimates it by about 5 m s^{-1}.

During this period, the surface is slightly warmer than the air above, indicating convective conditions in the boundary layer (note that the sea ice cover is less than 100% at this time, **Figure 3a**). This general structure is captured in the reanalysis, although the reanalysis temperatures are warmer than those observed by about 2°C. An earlier episode of observed convective conditions, after the sudden drop in temperature on April 16, is not seen in the reanalysis. During the initial days prior to the intrusion events, the reanalysis is about 5°C warmer than observations, and there is a lag in reanalysis temperature changes during the majority of the TOP. These surface temperature biases are most likely due to the simplified treatment of the sea ice in ERA5, which has a layer of ice with constant thickness and no insulating snow layer (Vihma et al., 2002; Batrak and Müller, 2019; Arduini et al., 2022).

Next, we examine cloud liquid and ice water paths as derived from remote sensing (**Table 2**) and from ERA5 (**Figure 4**) and how the phase of the clouds influences the surface energy budget (**Figure 5**). As the TOP was during polar day, solar radiation reaches the surface during all hours, although some of it is reflected/absorbed by liquid and ice clouds. The surface reflects the majority of incident solar radiation as the observed albedo is above 0.8 with no clear change during the TOP (not shown). Liquid and mixed-phase clouds (**Figure 4**) alter the downwelling longwave radiation substantially (**Figure 5**) and, as expected, reduce the net loss of energy at the surface. Combining the net radiative fluxes with the turbulent fluxes, we have the total energy budget at the surface where the net input of energy to the surface during these warm air advection events can clearly be seen (**Figure 6**).

Most of the time, the net energy in ERA5 agrees remarkably well with the observations. For the first 2 days, there is a net loss of energy at the surface with a clear diurnal cycle, with ERA5 showing about 20 W m^{-2} more surface cooling than the observations (**Figure 6**). The turbulent heat fluxes are generally quite small both in observations and ERA5 during these 2 days (**Figure 6a**) and not much cloud liquid or ice is present (**Figure 4**). On April 13 and 14, there are larger turbulent fluxes. The observations on April 13, however, show a downward sensible heat flux while ERA5 shows upward flux, with the opposite being true on April 14.

ERA5 has a sea ice concentration of unity up until late on April 13, and at this time, the sign of the turbulent sensible heat fluxes changes in both observations and ERA5. The sea ice concentration stays below unity during the whole first warm air intrusion, likely as a combined effect of wind-driven sea ice dynamics and the large downward sensible heat flux, particularly on April 16, preventing refreezing of leads probably opened by the wind (Aue et al., 2022). The ERA5 turbulent fluxes are substantially overestimated, which does not seem to be related to biases in wind shear (**Figure 3**). One contributing factor to the poor estimate of turbulent heat fluxes in ERA5 is likely to be the representation of scalar roughness over sea ice (Elvidge et al., 2021; Elvidge et al., 2023) as well as the fact that the observations and the reanalysis are differently influenced by the presence of leads. Nevertheless, the resulting net surface energy (radiative and turbulent fluxes) bias in the reanalysis, of about 50 W m^{-2}, is most

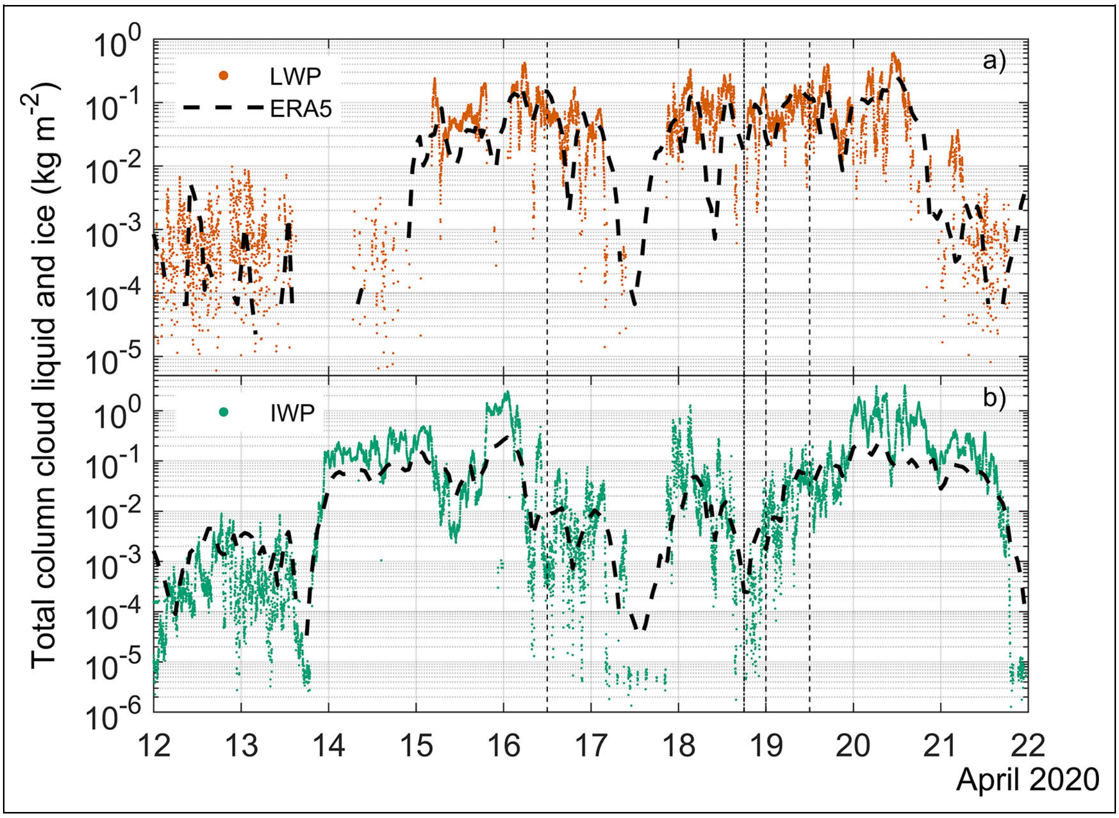

Figure 4. Observed (marker) and reanalysis (dashed line) liquid water path (kg m^{-2}, a) and ice water path (kg m^{-2}, b) during the targeted observing period (April 12–22, 2020). Note the logarithmic scale.

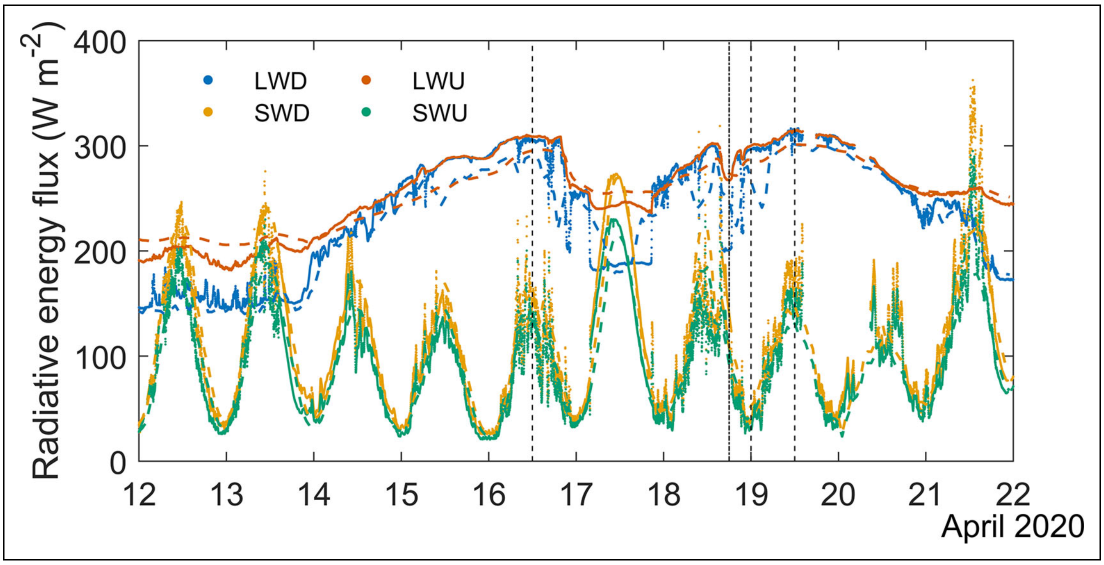

Figure 5. Observed (solid circles) and reanalysis (dashed line) components of the radiative fluxes (W m^{-2}) during the targeted observing period (April 12–22, 2020).

pronounced around the times of the maxima in surface temperature (**Figure 6**).

During the colder period between the two main warm air pulses, the sea ice concentration is unity again and there is a net loss of energy at the surface in both observations and reanalysis. During the following pulse of warm air, the turbulent fluxes are again overestimated by ERA5 leading to an excess input of energy to the surface. Interestingly, during the last 24 h of the event, the observations show larger upward turbulent sensible heat fluxes than the reanalysis although the latent heat flux is considerably overestimated in the reanalysis. This is during the period when the reanalysis wind speed is greater than the observations (**Figure 3b**) leading to more well-mixed conditions (**Figure 3a**) and less surface sensible heat flux despite the likely stronger turbulent mixing.

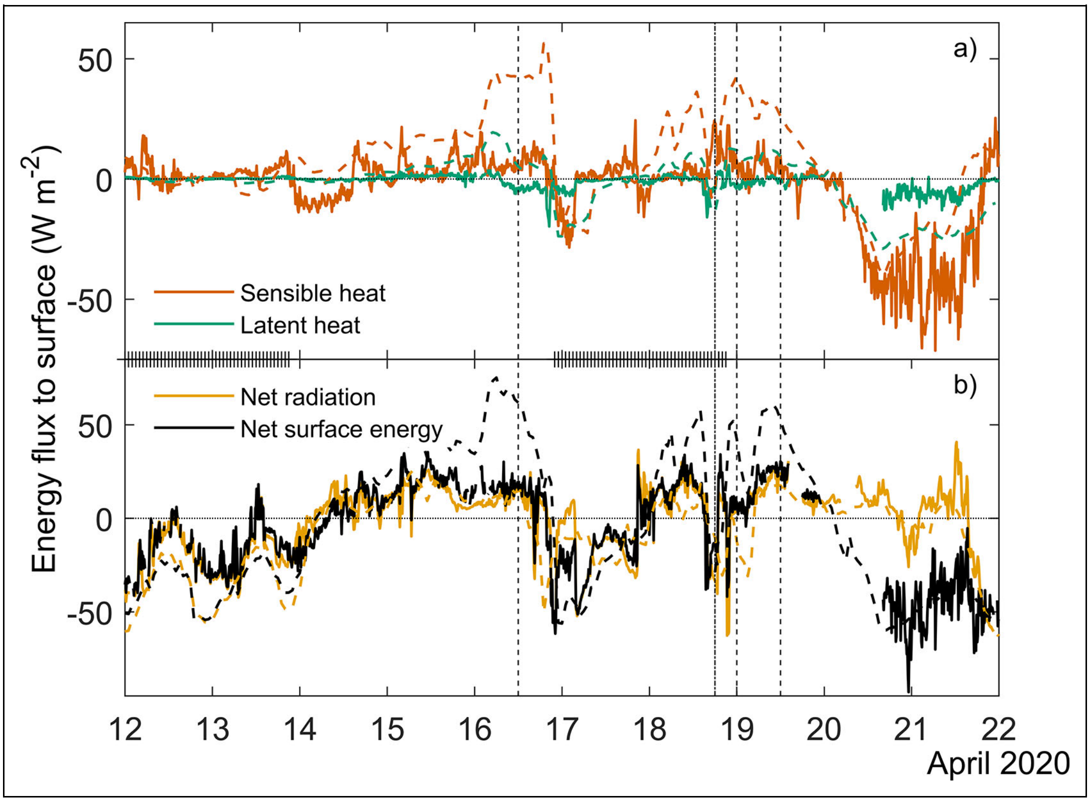

Figure 6. Observed (solid line) and reanalysis (dashed line) turbulent surface heat fluxes (W m^{-2}, a) and net surface radiative flux and net surface energy flux (sum of radiative and turbulent heat fluxes, W m^{-2}, b) during the targeted observing period (April 12–22, 2020). All fluxes are positive toward the surface. Sea ice cover of unity in the reanalysis is marked with symbols along the time axes in (a).

5.2. Vertical structure

The magnitudes of turbulent surface flux are the product of turbulence, which varies with the stability regime, and the near surface vertical gradients of temperature and specific humidity. Averaged over the whole TOP, the reanalysis agrees well with the observed vertical structure of temperature, humidity, and wind speed (black lines in **Figure 7**) above the local boundary layer, which is expected as the high-resolution soundings were assimilated. The mean profiles show the typical Arctic inversion with a maximum temperature in the 300–1,000 m layer and stable stratification below all the way to the surface in the reanalysis.

The observed mean profile and the reanalysis deviate from each other below 300 m, where the vertical structure is more important for the surface generated turbulence. The mean observed potential temperature structure is unstable below 40 m (not shown), a feature not seen in the reanalysis. During the coldest period, however, the lower layers are more stably stratified in the observations than in ERA5 (**Figure 7a**). Data assimilation influences the lower atmosphere less, so deviations are not surprising. Most pronounced is the difference in mean wind speed (**Figure 7c**), where ERA5 features higher wind speeds by about 2 m s^{-1} below 100 m; part of this could be the influence of flow distortion around the ship from which the soundings were released.

A closer look at the vertical structure at specific times during the TOP shows that all profiles have a temperature maximum at a height above 300 m as in the mean profile (**Figure 7**), but it is also clear that the vertical structure below this temperature maximum varies substantially and the bias in ERA5 is larger for the colder boundary layers. At the beginning of the TOP, the observed boundary layer is stably stratified, very cold and dry, and with weak winds. ERA5 is slightly warmer and has a well-mixed boundary layer.

There is the signature of a low-level cloud present in both observations and reanalysis, which agrees with the cloud ice and liquid water paths in **Figure 4**. The temperature and humidity profiles in the cloud layer are quite different and the reanalysis has an above-cloud moisture inversion that is too dry.

The first intrusion arrives at the MOSAiC site on April 16 and the 12 UTC sounding is warmer and moister than the mean profile below 3 km, with the maximum difference toward the surface in both observations and reanalysis. The observed wind profile has more shear than the reanalysis over the layer 30–200 m. This is in line with Jakobson et al. (2012), where 5 reanalyses show less shear than tethersonde data in the lowermost 120 m over Arctic Sea ice. All warm air intrusions come with stronger winds aloft. On April 16, the observations show a near-neutral layer closest to the surface, while there is a more complicated structure in the observations during April 19. The

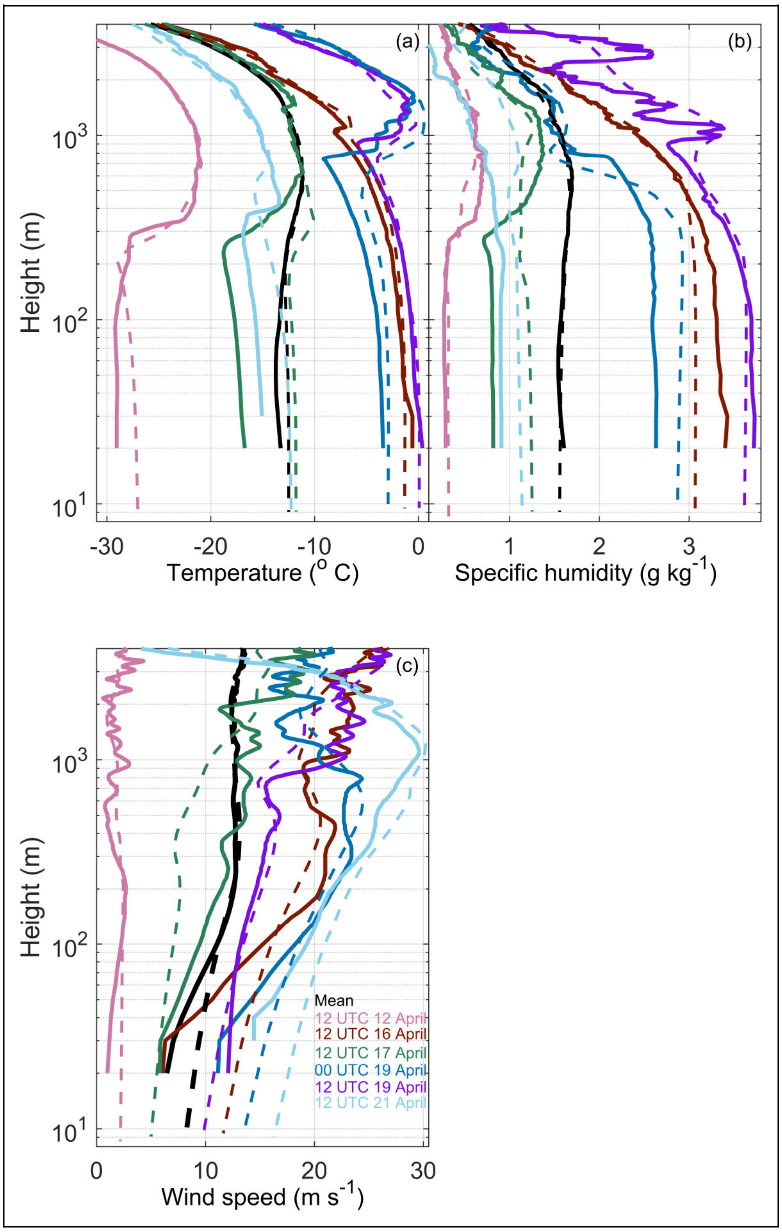

Figure 7. Observed (solid line) and reanalysis (dashed line) vertical profiles of temperature (°C, a), specific humidity (g kg^{-1}, b) and wind speed (m s^{-1}, c) at specific times (colors, see legend in c) and averaged (black) over the targeted observing period (April 12–22, 2020). Note the logarithmic scale.

warmer profiles are also moister, except for 00 UTC April 19 when the airmass passes over and descends in the lee of Greenland (see Section 4). The moisture content at that time is close to the average above 1 km, while below this height, the observed profiles show a clear increase in specific humidity and the signature of a cloud layer with cloud top cooling and a well-mixed wind profile between 300 and 800 m.

The 2 profiles on April 19 are both very warm above 1 km, but only the latter is moist. That profile has an increased moisture content in several distinct layers that are smeared out in the assimilation process in the reanalysis. The profiles at 12 UTC April 21 present big differences between the observations and reanalysis, especially in the upper part of the humidity profile. This is the period when the near surface variables also show biases (see Section 5.1).

The overall impression is that ERA5 is able to capture many of the observed temporal changes during the TOP, which indicates that the synoptic scale evolution is represented rather well. Even the temporal evolution in liquid and ice water paths is reproduced (**Figure 4**). When examining the magnitudes, it is clear that there are biases in cloud properties at times that then lead to biases in radiative fluxes. The largest biases are seen in the turbulent surface heat fluxes that at times have opposite signs (**Figure 6**). Part of these problems can be attributed to the simplified treatment of sea ice in ERA5 (Vihma et al., 2002; Batrak and Müller, 2019; Arduini et al., 2022) but possibly also to issues with representing the near surface vertical structure (e.g., Tjernström et al., 2021) or surface scalar exchange (e.g., Elvidge et al., 2021; Elvidge et al., 2023).

6. Lagrangian analysis of warm air pathways to the MOSAiC site

To further understand the history and transformation of the airmass that arrived at the MOSAiC site at a certain time, we analyze the interpolated column following one of the trajectories. **Figures 8–10** present the atmospheric column following the position of the back trajectories arriving at 800 hPa above MOSAiC at 12 UTC on April 16 and 00 and 12 UTC on April 19, respectively (orange lines, **Figure 2a**, **g**, and **j**). We follow the trajectories 48 h back in time and document the vertical displacement of the air parcel (black stars) as well as the diagnosed boundary layer height (dashed lines), terrain height (white area), and presence of sea-ice (black stars at sea level). Near-surface parameters, cloud liquid water and ice water paths, surface energy budget terms, and sea-ice concentration are also interpolated along the tracks (**Figure 11**).

As discussed in Section 4, the trajectories below 700 hPa follow approximately the same path for the final days before arriving at the MOSAiC site. The actual distance they travel can be quite different as the wind speed increases with height. Generally, the surface energy flux terms show the same variability over distance, regardless of the time they passed the same physical location (**Figure 12**). The exception is the solar radiation as it varies over the diurnal cycle. The same is not true for the integrated cloud water and ice content, which show more variation. The trajectories selected for the more detailed analysis are represented by the thicker lines in **Figure 12**, and the time axis for that trajectory is illustrated by the dashed vertical lines every 12 h. It is thus important to consider that the advective wind speed is quite different in time and among the 3 cases presented in **Figures 8–10**.

6.1. Trajectory ending at 12 UTC April 16, 2020

First, we follow the air column that reaches the MOSAiC site at 12 UTC on April 16 (**Figure 2a**) at the time of the first peak in near surface temperature (**Figure 3**). When the air leaves the Norwegian coast at about 42 h prior to arrival, the lowest 3 km of the atmosphere are warm, moist, and have liquid and ice clouds that are situated above the almost 1-km deep boundary layer (**Figure 8a** and **b**). Halfway to Svalbard, about 24 h before the arrival at the MOSAiC site, the clouds and humidity above the boundary layer decrease substantially due to precipitation (not shown), as evident in the integrated liquid and ice water content (**Figure 11a**). The Norwegian Sea is relatively warm; thus, the near surface temperature is well above zero (**Figures 8a** and **11a**).

The near surface moisture increases until the airmass passes over the marginal sea ice south of Svalbard, after which the near-surface temperature drops below freezing (**Figure 11a**). In this region, there is a low-level jet (**Figure 8c**), and when the air is forced to pass the rather steep terrain of Svalbard, clouds form but then evaporate on the lee side (**Figure 8b**). The near-surface temperature increases slightly with downslope flow in the lee of Svalbard but then cools as it moves further northward over the sea ice pack (**Figure 11a**).

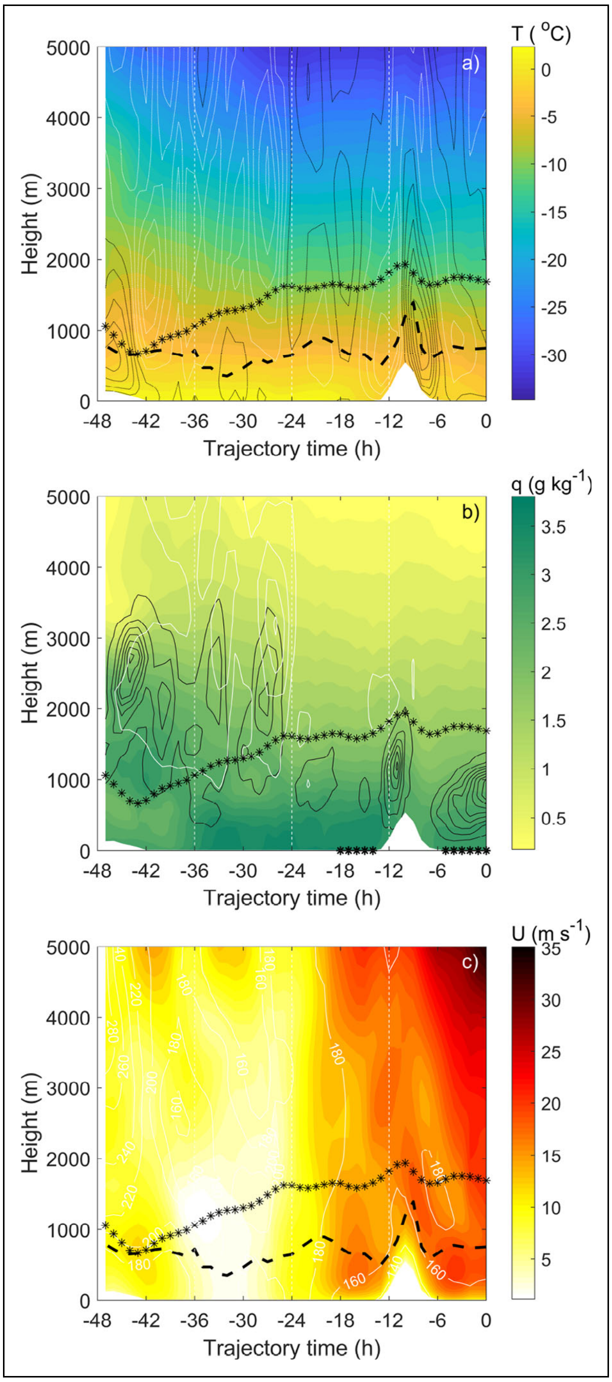

Figure 8. Contour plots along the back-trajectory initiated at 12 UTC April 16, 2020 for (a) temperature (°C), (b) specific humidity (g kg^{-1}) and cloud liquid and ice content (black and white contours, respectively, from 0.01 in intervals of 0.02 g kg^{-1}), and (c) wind speed (m s^{-1}) and wind direction (degrees, white contours). The air column is following the position of the trajectory initiated at 800 hPa (black stars) that changes altitude due to vertical motions (ω, Pa s^{-1}) with contour lines in panel (a) with white for upward motion and black for downward (intervals of 0.1 Pa). Also shown in all panels are the terrain height (white area), ERA5 diagnosed boundary-layer height (m, thick black dashed line) and white vertical dashed lines indicate noon and midnight UTC. Sea ice concentration above 0.15 is shown with black stars in (b).

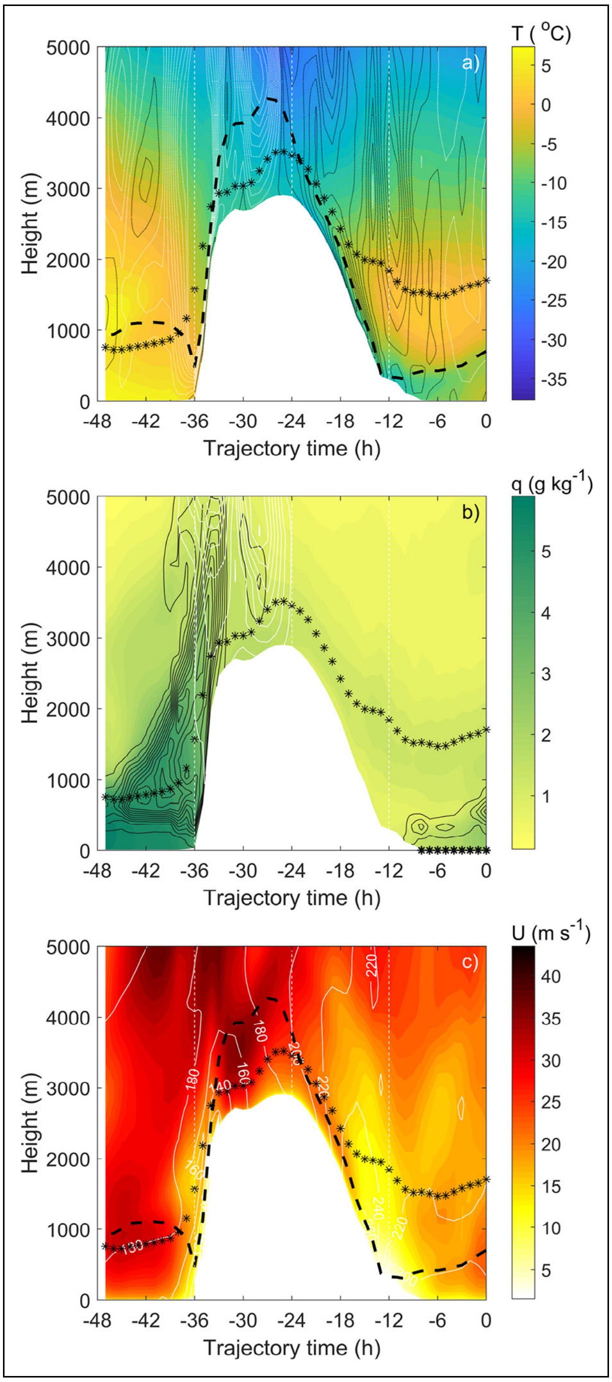

Figure 9. Contour plots along the back-trajectory initiated at 00 UTC April 19, 2020 for (a) temperature (°C), (b) specific humidity (g kg^{-1}) and cloud liquid and ice content (black and white contours, respectively, from 0.01 in intervals of 0.02 g kg^{-1}), and (c) wind speed (m s^{-1}) and wind direction (degrees, white contours). The air column is following the position of the trajectory initiated at 800 hPa (black stars) that changes altitude due to vertical motions (ω, Pa s^{-1}) with contour lines in panel (a) with white for upward motion and black for downward (intervals of 0.1 Pa). Also shown in all panels are the terrain height (white area), ERA5 diagnosed boundary-layer height (m, thick black dashed line) and white vertical dashed lines indicate noon and midnight UTC. Sea ice concentration above 0.15 is shown with black stars in (b).

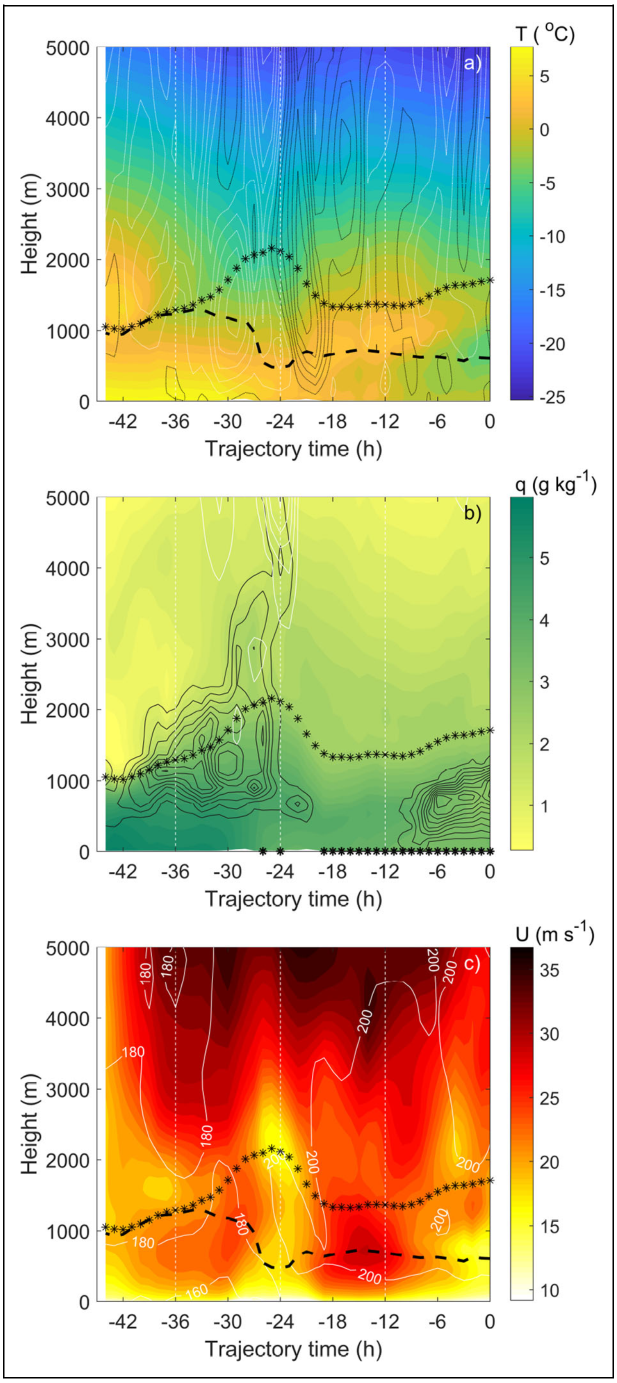

Figure 10. Contour plots along the back-trajectory initiated at 12 UTC April 19, 2020 for (a) temperature (°C), (b) specific humidity (g kg^{-1}) and cloud liquid and ice content (black and white contours, respectively, from 0.01 in intervals of 0.02 g kg^{-1}), and (c) wind speed (m s^{-1}) and wind direction (degrees, white contours). The air column is following the position of the trajectory initiated at 800 hPa (black stars) that changes altitude due to vertical motions (ω, Pa s^{-1}) with contour lines in panel (a) with white for upward motion and black for downward (intervals of 0.1 Pa). Also shown in all panels are the terrain height (white area), ERA5 diagnosed boundary-layer height (m, thick black dashed line) and white vertical dashed lines indicate noon and midnight UTC. Sea ice concentration above 0.15 is shown with black stars in (b).

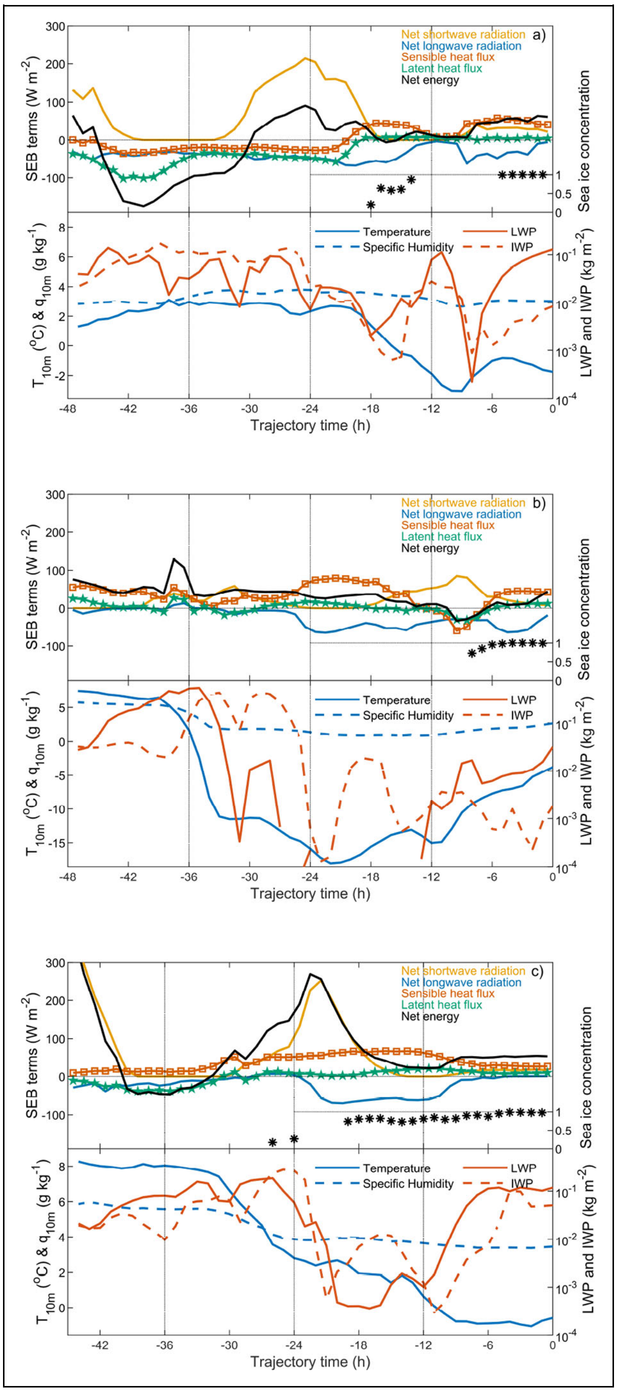

Figure 11. Components of (color) and net (black) surface energy budget (left top axis, W m^{-2}), sea ice concentration (black stars, right top axis), temperature and specific humidity at 10 m (left bottom axis, °C and g kg^{-1}, respectively), and liquid and ice water paths (right bottom axis, kg m^{-2}) along back trajectories originating at 800 hPa on (a) 12 UTC April 16, (b) 00 UTC April 16, and (c) 12 UTC April 19. Note that the axes are different. The symbols illustrate the 1-h resolution of the data.

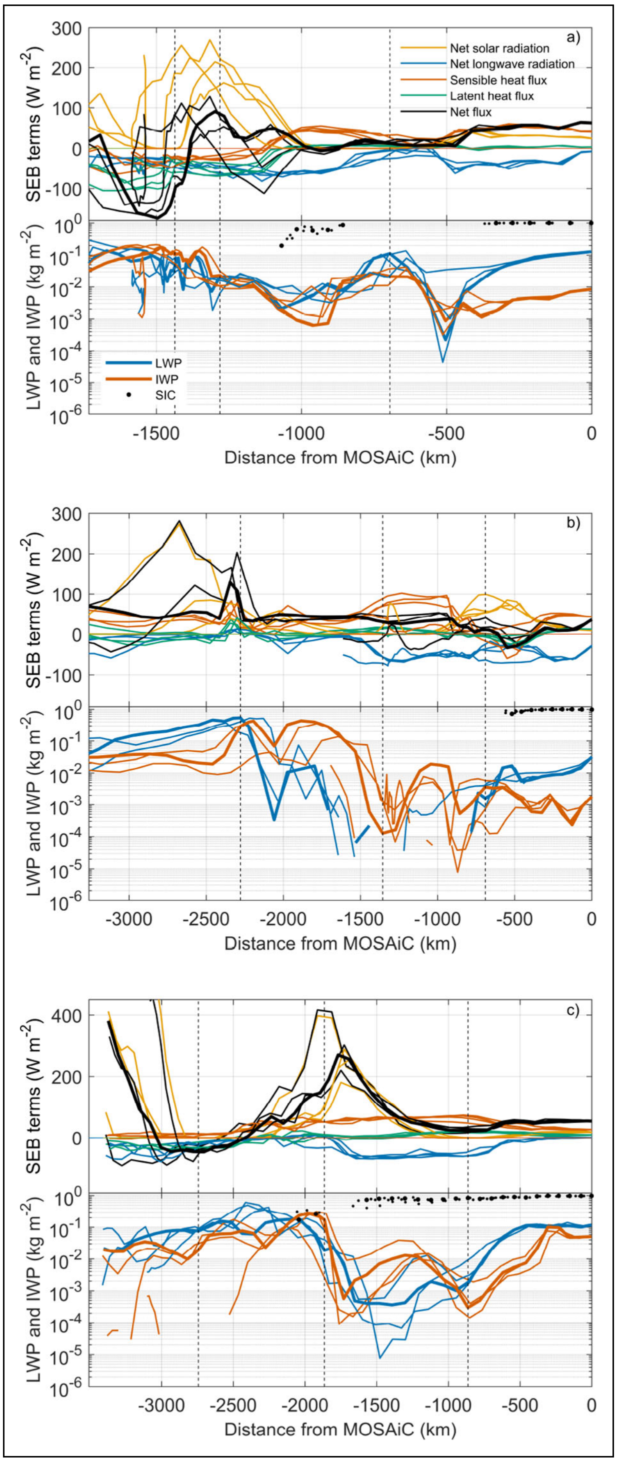

Figure 12. Components of (color) and net (black) surface energy budget (upper panel, W m^{-2}) and liquid and ice water paths (lower panel, kg m^{-2}) along with sea ice concentration plotted with distance from the initial point at 700, 800, 850, and 900 hPa on (a) 12 UTC April 16, (b) 00 UTC April 16, and (c) 12 UTC April 19. The thick line and larger marker for the sea ice concentration are for the trajectory originating at 800 hPa, that is, the same as in **Figure 11**.

During the last 6 h before reaching the MOSAiC site, a mostly liquid cloud forms below about 1 km, and the atmospheric temperature decreases but the boundary layer stays rather deep as the winds are fairly strong (**Figure 8b** and **c**). The thick clouds block much of the incident solar radiation, such that shortwave and longwave radiative fluxes effectively balance each other (**Figure 11a**). As a result, the large sensible heat flux is approximately equal to the net surface energy flux, with a substantial positive input to the surface for this stretch over sea ice. The latent heat flux is generally small over the sea ice but larger over the Nordic Seas, where weak winds lead to slow airmass advection (**Figures 11a** and **12a**).

Overall, the underlying surface seems to strongly determine the net energy budget, especially over the sea ice between the MOSAiC site and Svalbard. However, the exact path that the airmass takes over Svalbard results in differences in the integrated cloud liquid water and its influence on the net longwave radiation is substantial (**Figure 12a**).

6.2. Trajectory ending at 00 UTC April 19, 2020

Two days before the arrival at the MOSAiC site during the second episode, the 800 hPa trajectory is well south of Greenland (**Figure 2g**). The advection is fast until it crosses the coastline at about −36 h; then, the airmass takes about 12 h to reach the summit (**Figure 9c**), which is a distance of about 900 km (**Figure 12**). The air that reaches Greenland is warm and moist with deep liquid clouds that precipitate out much of the column water as the airmass ascends the slope (**Figure 9a** and **b**).

The diagnosed boundary layer is very shallow going up the slope. The wind speed increases at the top of the ice sheet, and the sensible heat input to the surface increases from an already rather high positive value (**Figures 11b** and **12b**). On the down-slope side, the atmospheric column is considerably drier, and the clouds are almost dissipated, but a layer with very warm air between 1 and 2 km remains. The wind weakens during this downslope flow, and as a result, the boundary layer becomes extremely shallow again with diminishing turbulent heat fluxes.

Near the coastal transition, the negative net longwave radiation is balanced by the solar radiation, resulting in a net energy budget near zero. Once the airmass reaches the broken sea ice north of Greenland, the sensible and latent turbulent fluxes provide heat and moisture to the lower layers (**Figure 11b**). Extending north from that point, a boundary layer liquid cloud is formed, and the turbulent fluxes shift sign and the net energy becomes positive (**Figures 9b** and **11b**). The trajectories passing over Greenland have more variation in the surface energy budget terms and, the cloud liquid and ice water paths, than the ones passing over the ocean (**Figure 12b**), however, north of the land mass, they all converge.

Once the airmass reaches the location of MOSAiC, there is still a warm (but dry) layer between 1 and 2 km (**Figure 7a** and **b**) that originated from the very warm and moist low-level airmass south of Greenland. The boundary layer moistening below approximately 800 m at the MOSAiC site seems to come from a longer path trajectory at lower levels that flows over the partly ice-covered ocean (green trajectory in **Figure 2g**). It is most likely the lower cloud that causes the observed increase in downwelling longwave radiation (**Figure 5**).

6.3. Trajectory ending at 12 UTC April 19, 2020

At the time of the maximum observed temperature at midday on April 19 (**Figure 3**), the rapid transport is from the south along the Greenland coast (**Figure 2j**). The air is warm and moist both near the surface and in a layer above the boundary layer (**Figure 10a** and **b**) at the MOSAiC site (**Figure 7**). The advection is so fast that the trajectory initiated at 800 hPa is outside of the area of interest already at −45 hours, covering almost 4,000 km, while the previously discussed airmasses travel considerably shorter distances over the same time (**Figure 12**). Again, the correspondence of the surface energy budget terms with the underlying surface is evident and the fetch over sea ice is much longer (**Figure 12c**).

The vertical wind field is also variable and closer examination reveals that the trajectory actually passes over coastal land twice between −30 and −18 h (**Figure 10a**), over the western edge of Iceland and the Greenland coast (**Figure 2j–l**). The trajectory lifts about 1,000 m before −24 h and the clouds (mostly liquid) deepen to 5 km before evaporating (**Figure 10b**) in the strong subsidence region between −24 and −18 h (**Figure 10a**). The boundary layer depth also changes considerably from >1 km depth in the south to about half of that in the north (**Figure 10**) with a minimum in between coinciding with lower wind speeds (**Figure 10c**).

During the last 10 h before arriving at the MOSAiC site, a low-level liquid cloud is present. It cools radiatively but not enough to make the whole layer below turbulent in ERA5 (not shown). Near-surface layers remain stably stratified along the entire trajectory with substantial downward sensible heat fluxes. There is a considerable net energy input to the surface over the sea ice when the low cloud reduces the surface cooling, which results in a net longwave radiation close to zero and only a small contribution from the shortwave radiation (**Figure 11c**).

6.4. Matching trajectories with soundings ending at 18 UTC April 18, 2020

Following a trajectory back in time, comparisons against observations are possible when it passes over or near observational sites, such as the sounding stations mentioned in Section 4. The time of focus here aligns with a brief temperature decrease during the second warm episode (**Figure 3**), and with the fortuitous passing of the trajectory over 4 sounding stations at different stages of the airmass transformation process (**Figure 13**). The airmasses pass over Greenland (**Figure 13c**) and those at 700 and 800 hPa travel quite similar paths, both passing over Tasiilaq when crossing the coastline, but with different speeds.

The profiles upstream of Greenland show a warm and moist marine airmass, except for the near-surface layer where the observations are influenced by the most likely snow-covered land surface (**Figure 13**). When reaching Summit station, most of the moisture has been removed and the air has less than 1 g kg^{-1} of water vapor and temperatures below −20°C. The 700 hPa trajectory's closest match at this sounding time is further north (**Figure 13c**) and has the same vertical structure but is warmer and moister (**Figure 13a** and **b**). Both ERA5 profiles show

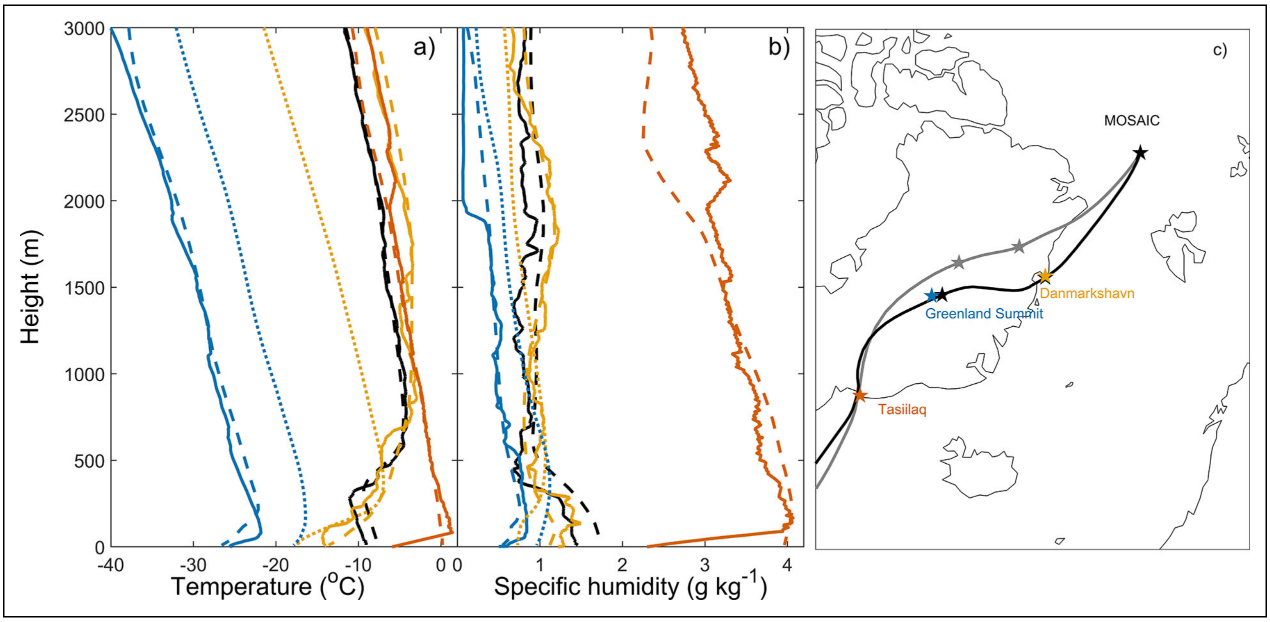

Figure 13. Vertical profiles of (a) temperature (°C) and (b) specific humidity (g kg^{-1}) at times when back trajectories originating at 700 (dotted) and 800 hPa (dashed) at 18 UTC on April 18, 2020 pass close (gray and black lines and stars for trajectories originating at 700 and 800 hPa) in panel c, respectively, to the observational stations (colored stars). The solid lines in panels (a) and (b) are observations at the MOSAiC (black) and the sounding stations colored as in panel (c).

surface inversions, as indicated by the observations, but they are deeper and less defined and without the observed low-level jet (not shown).

Right before the 800-hPa trajectory leaves Greenland at Danmarkshavn (**Figure 13c**), the temperatures are considerably warmer due to the subsiding motion, but the specific humidity values remain about 1 g kg^{-1}. The more northerly trajectory is still some distance from the coast where the profile is now generally colder and drier. Both ERA5 profiles show surface inversions while the observations show a shallow well-mixed boundary layer below 100 m. Finally at the MOSAiC site, there is indication of a well-mixed, likely cloud topped, boundary layer in both observations and ERA5 with a slight increase in the humidity below 500 m. ERA5 is both warmer and moister in this layer.

The overall good agreement between the observed and ERA5 profiles is not surprising as they are not independent data. There are differences in the boundary layer structures, which in turn influence the stability and thereby the turbulent fluxes at the surface. The analysis along the trajectory clearly shows that the airmass transformation is quite dramatic when the air passes over Greenland in a föhn type of flow.

7. Conclusions

Meridional transport of heat to the high Arctic is a necessary component of the climate system. The episodic transport that brings warm, and often moist, air to the region has implications for the coupled atmosphere-sea ice-ocean system. An interesting period of such episodes, April 12–22, 2020, is defined as a YOPP TOP during the MOSAiC year (Shupe et al., 2022). This period represents the first time during the spring of 2020 that the atmospheric circulation favors meridional transport from the Atlantic. During these episodes, surface temperature near the melting point was observed, though this was not the start of the persistent sea ice melt season. The period did, however, mark a transition from a cold, winter regime with temperatures considerably below −20°C to a spring transition season with temperatures typically above −20°C (e.g., Shupe et al., 2022).

The period is analyzed using a Lagrangian perspective with the aim to find novel ways to evaluate and improve weather forecast and climate models in polar regions as discussed in Pithan et al. (2018). In this case, fortuitous comparisons of the airmass transformation processes at multiple points along Lagrangian trajectories provide strong context for downstream evaluation of more detailed processes (clouds, energy fluxes) at a fixed location.

A large-scale analysis combining trajectories, cyclone tracks, and blocking frequencies illustrates the components of the flow that allow for rapid meridional transport of warm and moist air to the Arctic. Typically, a dipole pressure pattern forms an advection corridor that guides the air. It is interesting to see that the transport, as depicted by back trajectories initiated at different heights from the surface to 700 hPa, follows the same general path. This feature allows for analysis of column airmass transformations along one of the trajectories. This vertical alignment prior to entering the high Arctic has been noted before (e.g., Ali and Pithan, 2020) and the mechanisms facilitating this merit further investigation.

The airmasses leading to the first temperature peak at the MOSAiC site on April 16 take a route across the

Atlantic, turning at the Norwegian coast and then crossing the Nordic Seas before reaching the observational site. Analysis of the column following the position of the back trajectory initiated at 800 hPa shows an airmass that is moist and warm in the lower 3–4 km when leaving the Norwegian coast. More moisture and heat are added to the airmass as it moves north from the relatively warmer ocean, before the near-surface cooling intensifies when the airmass advects over the sea ice and a low-level cloud forms.

After the first event, the temperature at the MOSAiC site temporarily drops as the site is influenced by air that has resided over the ice for a longer time. The large-scale pressure dipole shifts more to the west and an advection path sets up from the south and across Greenland pointing to the MOSAiC site. As the air passes over the ice sheet, clouds form and moisture precipitates out, which results in a warm, yet dry, airmass that leaves the northern edge of Greenland. Once the airmass is over the ocean and the marginal sea ice zone, the lower portion of the air becomes moister and a shallow liquid cloud forms. The surface warms due to increased longwave radiation to the surface from clouds.

Over the following 12 h, the large-scale circulation shifts slightly, so that the meridional flow now is over the mostly sea ice covered ocean along the east Greenland coast. This circulation pattern leads to the highest surface temperatures observed during the YOPP TOP at the MOSAiC site, almost triggering surface melt. The air is warm and moist in a much deeper layer than earlier in the period.

The analysis along trajectories is based on ERA5 reanalysis fields. Some variables are qualitatively evaluated using observations at the MOSAiC site and at a few other sounding stations along the airmass trajectories. The vertical structure of the state variables, temperature, humidity, and wind speed and direction, are generally well captured, although differences are larger in the boundary layer, possibly partly explained by the coastal locations of the sounding stations with contrasting surface conditions. The temporal evolution of the wind speed and direction agrees well with observations at the MOSAiC site even though the thermodynamic variables have considerable biases and the sensible heat flux is substantially overestimated around the times of maximum advection of warm air.

The presented time period is dynamically quite active and thus challenging for models to represent properly. Nevertheless, as the analyzed trajectories do line up vertically, we propose that airmass transformation can be studied in a Lagrangian framework during this case as suggested in Pithan et al. (2018). This perspective provides information on how processes evolve with time, something that is not possible to address with observations at only 1 location.

Further study of the YOPP TOP is motivated by a range of scientific questions and already established issues with the representation of small-scale processes in numerical weather prediction and climate models. These are related to representing the fractional ice, snow on land and ice, surface turbulent fluxes, cloud and cloud phase, and their impact on radiation, vertical structure in atmosphere and upper ocean (e.g., Vihma et al., 2002; Svensson and Karlsson, 2011; Holtslag et al., 2013; Ilcak et al., 2016; Pithan et al., 2016; Elvidge et al., 2021; Inoue et al., 2021; Renfrew et al., 2021; Tjernström et al., 2021; Solomon et al., 2023). A wealth of additional process observations are available from key projects like MOSAiC (Shupe et al., 2022) and COMBLE (Geerts et al., 2022), as well as long-term research stations Sodankylä, Greenland Summit station, and Ny Ålesund, which combined with additional TOP trajectories that pass over these locations provide unique opportunities for novel model analyses and provide a valuable step toward improving numerical weather prediction and climate models.

The overall performance of the state-of-the-art numerical weather prediction and climate models depends on how the various parameterizations act together, how they are coupled to the dynamical core, and all techniques utilized to numerically solve the complex system. The evaluation of these convoluted codes, while aiming for improved process representation, calls for new methodologies and tools, such as coupled single column models (AOSCMs, e.g., Hartung et al., 2018), nudged climate model simulations (e.g., Pithan et al., 2022), and more advanced Lagrangian analysis as presented here following the ideas in Pithan et al. (2018). The impact of these complex dynamical situations, with their resulting meridional flow, is important for the representation of Arctic climate (e.g., Murto, 2022) and climate change (e.g., Pithan and Mauritsen, 2014). These are also the situations when numerical weather prediction forecasts are very sensitive to observational coverage in the Euro-Arctic (e.g., Day et al., 2019).

Data accessibility statement

Observational data were collected as part of the international Multidisciplinary drifting Observatory for the Study of Arctic Climate (MOSAiC) with tags MOSAiC20192020 and AWI–PS122–00. Surface meteorology and turbulent heat fluxes were measured by the University of Colorado/NOAA surface flux team and are available for download from the Arctic Data Center (https://arcticdata.io). Surface radiation measurements were obtained from the Atmospheric Radiation Measurement (ARM) User Facility, a U.S. Department of Energy Office of Science User Facility Managed by the Biological and Environmental Research Program. The Cold-Air Outbreaks in the Marine Boundary Layer Experiment and Greenland summit data are also available for download from the ARM Archive (https://www.arm.gov/data). The ERA5 reanalysis fields are available from the Copernicus Climate Data Store (https://cds.climate.copernicus.eu).

Supplemental files

The supplemental files for this article can be found as follows:

The analysis of the large-scale circulation in Section 4 is supported by additional Figures S1–S4 that show the 4-day evolution per half-a-day time steps leading up to the situations presented in **Figure 2**.

Acknowledgments

We acknowledge the European Centre for Medium-range Weather Forecasts for providing the ERA5 data set and adopting some of their forecast products for the Arctic. Maxi Böttcher (ETH, Zürich) is acknowledged for providing on-demand forecast trajectories during the experimental phase. Support from the Steering groups of World Weather Research Program Polar Prediction Project and Multidisciplinary Drifting Observatory for the Study of Arctic Climate (MOSAiC) is acknowledged, in particular members of the YOPP polar processes task team. Support for the extra soundings is acknowledged from Alfred Wegener Institute (AWI), Danish Meteorological Institute (DMI), U.S. Department of Energy (DOE), Environment and Climate Change Canada (ECCC), Finnish Meteorological Institute (FMI), Icelandic Meteorological Office (IMO), MetNorway, and SMHI as well as the COMBLE team. We also thank Jakob Beran (Stockholm University) for providing the cyclone tracks and Lukas Papritz (ETH, Zürich) for detecting atmospheric blocks and helping with the LAGRANTO Tool for computing trajectories using ERA5 data.

Funding

Summit station radiosondes were supported by the National Science Foundation (NSF) under OPP-1801477. JJD was supported by European Union's Horizon 2020 Research and Innovation program through Grant Agreement 871120 (INTERACTIII) and TV under Grant agreement no. 101003590 (PolarRES). JDD was supported by the Office of Naval Research Arctic Cyclone DRI program element 0602435 N. MDS was supported by the NSF (OPP-1724551), DOE Atmospheric System Research Program (DE-SC0021341), and the NOAA Global Ocean Monitoring and Observing program (via NA22OAR4320151). IAR acknowledge NERC NE/N009754/1 (Iceland Greenland Seas Project) and NE/S000453/1 (CANDIFLOS). TS was supported by Research Council of Norway, project ARCLINK (project number: 328938). SM was funded by Knut och Alice Wallenbergs Stiftelse, grant 2016-0024. Some of the trajectory computations were enabled by resources provided by the Swedish National Infrastructure for Computing, partially funded by the Swedish Research Council through grant agreement no. 2018-05973.

Competing interests

All authors declare that they have no competing interests. MDS is a guest editor for the Elementa Special Feature on Multidisciplinary drifting Observatory for the Study of Arctic Climate but was not involved in the editorial or review process for this manuscript.

Author contributions

The extra observations during the targeted observing period were coordinated by GS with support from members of the YOPP Process Task Team. GS also designed the study, did most of the analysis, and wrote the majority of the text. SM contributed the trajectory calculations using the reanalysis fields and the large-scale analysis which is summarized in Section 4. LM provided sounding data retrieved from the Global Telecommunications System archive at European Centre for Medium-range Weather Forecasts. MDS coordinated the atmospheric program during Multidisciplinary drifting Observatory for the Study of Arctic Climate from which the site observations are obtained. All authors contributed by reading, editing, and commenting on the manuscript.

References

Ali, SM, **Pithan, F.** 2020. Following moist intrusions into the Arctic using SHEBA observations in a Lagrangian perspective. *Quarterly Journal of the Royal Meteorological Society* **146**(732): 3522–3533. DOI: http://dx.doi.org/10.1002/qj.3859.

Arduini, G, **Keeley, S**, **Day, JJ**, **Sandu, I**, **Zampieri, L**, **Balsamo, G.** 2022. On the importance of representing snow over sea-ice for simulating the Arctic boundary layer. *Journal of Advances in Modeling Earth Systems* **14**(7): e2021MS002777. DOI: http://dx.doi.org/10.1029/2021MS002777.

Aue, L, **Vihma, T**, **Uotila, P**, **Rinke, A.** 2022. New insights into cyclone impacts on sea ice in the Atlantic sector of the Arctic Ocean in winter. *Geophysical Research Letters* **49**(22): e2022GL100051. DOI: http://dx.doi.org/10.1029/2022GL100051.

Batrak, Y, **Müller, M**. 2019. On the warm bias in atmospheric reanalyses induced by the missing snow over Arctic sea-ice. *Nature Communications* **10**(1): 1–8. DOI: http://dx.doi.org/10.1038/s41467-019-11975-3.

Bengtsson, L, **Hodges, KI**, **Koumoutsaris, S**, **Zahn, M**, **Keenlyside, N.** 2011. The changing atmospheric water cycle in Polar Regions in a warmer climate. *Tellus A* **63**(5): 907–920. DOI: http://dx.doi.org/10.1111/j.1600-0870.2011.00534.x.

Cox, C, **Gallagher, M**, **Shupe, M**, **Persson, O**, **Solomon, A**, **Blomquist, B**, **Brooks, I**, **Costa, D**, **Gottas, D**, **Hutchings, J**, **Osborn, J**, **Morris, S**, **Preusser, A**, **Uttal, T**. 2021. 10-meter meteorological flux tower measurements (Level 1 Raw), Multidisciplinary Drifting Observatory for the Study of Arctic Climate (MOSAiC), central Arctic, October 2019–September 2020. Arctic Data Center. DOI: http://dx.doi.org/10.18739/A2VM42Z5F.

Cox, C, **Gallagher, M**, **Shupe, M**, **Persson, O**, **Solomon, A**, **Fairall, CW**, **Ayers, T**, **Blomquist, B**, **Brooks, IM**, **Costa, D**, **Grachev, A**, **Gottas, D**, **Hutchings, JK**, **Kutchenreiter, M**, **Leach, J**, **Morris, SM**, **Morris, V**, **Osborn, J**, **Pezoa, S**, **Preusser, A**, **Riikimaki, LD**, **Uttal, T**. n.d. Continuous observations of the surface energy budget and meteorology over the Arctic Sea ice during MOSAiC. *Scientific Data,* submitted, under review.

Croci-Maspoli, M, **Schwierz, C**, **Davies, H**. 2007. A multifaceted climatology of atmospheric blocking and its recent linear trend. *Journal of Climate* **20**(4): 633–649. DOI: http://dx.doi.org/10.1175/JCLI4029.1.

Dada, L, **Angot, H**, **Beck, I**, **Baccarini, A**, **Quéléver, LLJ**, **Boyer, M**, **Laurila, T**, **Brasseur, Z**, **Jozef, G**, **de Boer, G**, **Shupe, MD**, **Henning, S**, **Bucci, S**, **Dütsch,**

M, **Stohl, A**, **Petäjä, T**, **Daellenbach, KR**, **Jokinen, T**, **Schmale, J**. 2022. A central Arctic extreme aerosol event triggered by a warm air-mass intrusion. *Nature Communications* **13**. DOI: http://dx.doi.org/10.1038/s41467-022-32872-2.

Day, JJ, **Sandu, I**, **Magnusson, L**, **Rodwell, MJ**, **Lawrence, H**, **Bormann, N**, **Jung, T**. 2019. Increased Arctic influence on the midlatitude flow during Scandinavian blocking episodes. *Quarterly Journal of the Royal Meteorological Society* **145**(725): 3846–3862. DOI: http://dx.doi.org/10.1002/qj.3673.

Dufour, A, **Zolina, O**, **Gulev, SK**. 2016. Atmospheric moisture transport to the Arctic: Assessment of reanalyses and analysis of transport components. *Journal of Climate* **29**(14): 5061–5081. DOI: http://dx.doi.org/10.1175/JCLI-D-15-0559.1.

Elvidge, AD, **Renfrew, IA**, **Brooks, IM**, **Srivastava, P**, **Yelland, MJ**, **Prytherch, J**. 2021. Surface heat and moisture exchange in the marginal ice zone: Observations and a new parameterization scheme for weather and climate models. *Journal of Geophysical Research: Atmospheres* **126**(17): e2021JD034827. DOI: http://dx.doi.org/10.1029/2021JD034827.

Elvidge, AD, **Renfrew, IA**, **Edwards, JM**, **Brooks, IM**, **Srivastava, P**, **Weiss, AI.** 2023. Improved simulation of the polar atmospheric boundary layer by accounting for aerodynamic roughness in the parameterisation of surface scalar exchange over sea ice. *Journal of Advances in Modeling Earth Systems* **15**. DOI: http://dx.doi.org/10.1029/2022MS003305.

Fearon, MG, **Doyle, JD**, **Ryglicki, DR**, **Finocchio, PM**, **Sprenger, M**. 2021. The role of cyclones in moisture transport into the Arctic. *Geophysical Research Letters* **48**(4): e2020GL090353. DOI: http://dx.doi.org/10.1029/2020GL090353.

Geerts, B, **Giangrande, SE**, **McFarquhar, GM**, **Xue, L**, **Abel, SJ**, **Comstock, JM**, **Crewell, S**, **DeMott, PJ**, **Ebell, K**, **Field, P**, **Hill, TCJ**, **Hunzinger, A**, **Jensen, MP**, **Johnson, KL**, **Juliano, TW**, **Kollias, P**, **Kosovic, B**, **Lackner, C**, **Luke, E**, **Lüpkes, C**, **Matthews, AA**, **Neggers, R**, **Ovchinnikov, M**, **Powers, H**, **Shupe, MD**, **Spengler, T**, **Swanson, BE**, **Tjernström, M**, **Theisen, AK**, **Wales, NA**, **Wang, Y**, **Wendisch, M**, **Wu, P**. 2022. The COMBLE Campaign: A study of marine boundary layer clouds in Arctic cold-air outbreaks. *Bulletin of the American Meteorological Society* **103**(5): E1371–E1389. DOI: http://dx.doi.org/10.1175/BAMS-D-21-0044.1.

Goosse, H, **Kay, JE**, **Armour, KC**, **Bodas-Salcedo, A**, **Chepfer, H**, **Docquier, D**, **Jonko, A**, **Kushner, PJ**, **Lecomte, O**, **Massonnet, F**, **Park, H-S**, **Pithan, F**, **Svensson, G**, **Vancoppenolle, M**. 2018. Quantifying climate feedbacks in polar regions. *Nature Communications* **9**(1): 1–13. DOI: http://dx.doi.org/10.1038/s41467-018-04173-0.

Graham, RM, **Cohen, L**, **Ritzhaupt, N**, **Segger, B**, **Graversen, RG**, **Rinke, A**, **Walden, VP**, **Granskog, MA**, **Hudson, SR**. 2019a. Evaluation of six atmospheric reanalyses over Arctic Sea ice from winter to early summer. *Journal of Climate* **32**(14): 4121–4143. DOI: http://dx.doi.org/10.1175/JCLI-D-18-0643.1.

Graham, RM, **Hudson, SR**, **Maturilli, M**. 2019b. Improved performance of ERA5 in Arctic gateway relative to four global atmospheric reanalyses. *Geophysical Research Letters* **46**(11): 6138–6147. DOI: http://dx.doi.org/10.1029/2019GL082781.

Hartung, K, **Svensson, G**, **Struthers, H**, **Deppenmeier, AL**, **Hazeleger, W.** 2018. An EC-Earth coupled atmosphere–ocean single-column model (AOSCM.v1_EC-Earth3) for studying coupled marine and polar processes. *Geoscientific Model Development* **11**(10): 4117–4137. DOI: http://dx.doi.org/10.5194/gmd-11-4117-2018.

Hersbach, H, **Bell, B**, **Berrisford, P**, **Hirahara, S**, **Horányi, A**, **Muñoz-Sabater, J**, **Nicolas, J**, **Peubey, C**, **Radu, R**, **Schepers, D**, **Simmons, A**, **Soci, C**, **Abdalla, S**, **Abellan, X**, **Balsamo, G**, **Bechtold, P**, **Biavati, G**, **Bidlot, J**, **Bonavita, M**, **De Chiara, G**, **Dahlgren, P**, **Dee, D**, **Diamantakis, M**, **Dragani, R**, **Flemming, J**, **Forbes, R**, **Fuentes, M**, **Geer, A**, **Haimberger, L**, **Healy, S**, **Hogan, RJ**, **Hólm, E**, **Janisková, M**, **Keeley, S**, **Laloyaux, P**, **Lopez, P**, **Lupu, C**, **Radnoti, G**, **de Rosnay, P**, **Rozum, I**, **Vamborg, F**, **Villaume, S**, **Thépaut, J-N**. 2020. The ERA5 global reanalysis. *Quarterly Journal of the Royal Meteorological Society* **146**(730): 1999–2049. DOI: http://dx.doi.org/10.1002/qj.3803.

Holtslag, AAM, **Svensson, G**, **Baas, P**, **Basu, S**, **Beare, B**, **Beljaars, ACM**, **Bosveld, FC**, **Cuxart, J**, **Lindvall, J**, **Steeneveld, GJ**, **Tjernström, M**, **Wiel, BJHVD.** 2013. Stable atmospheric boundary layers and diurnal cycles: Challenges for weather and climate models. *Bulletin of the American Meteorological Society* **94**(11): 1691–1706. DOI: http://dx.doi.org/10.1175/BAMS-D-11-00187.1.

Ilcak, M, **Drange, H**, **Wang, Q**, **Gerdes, R**, **Aksenov, Y**, **Bailey, D**, **Bentsen, M**, **Biastoch, A**, **Bozec, A**, **Böning, C**, **Cassou, C**, **Chassignet, E**, **Coward, AC**, **Curry, B**, **Danabasoglu, G**, **Danilov, S**, **Fernandez, E**, **Fogli, PG**, **Fujii, Y**, **Griffies, SM**, **Iovino, D**, **Jahn, A**, **Jung, T**, **Large, WG**, **Lee, C**, **Lique, C**, **Lu, J**, **Masina, S**, **George Nurser, A**, **Roth, C**, **Salas y Mélia, D**, **Samuels, BL**, **Spence, P**, **Tsujino, H**, **Valcke, S**, **Voldoire, A**, **Wang, X**, **Yeager, SG**. 2016. An assessment of the Arctic Ocean in a suite of Interannual CORE-II Simulations. Part III: Hydrography and fluxes. *Ocean Modelling* **100**: 141–161. DOI: http://dx.doi.org/10.1016/j.ocemod.2016.02.004.

Ingleby, B, **Candy, B**, **Eyre, J**, **Haiden, T**, **Hill, C**, **Isaksen, L**, **Kleist, D**, **Smith, F**, **Steinle, P**, **Taylor, S**, **Tennant, W**, **Tingwell, C**. 2021. The impact of COVID-19 on weather forecasts: A balanced view. *Geophysical Research Letters* **48**(4): e2020GL090699. DOI: http://dx.doi.org/10.1029/2020GL090699.

Inoue, J, **Sato, K**, **Rinke, A**, **Cassano, JJ**, **Fettweis, X**, **Heinemann, G**, **Matthes, H**, **Orr, A**, **Phillips, T**, **Seefeldt, M**, **Solomon, A**, **Webster, S**. 2021. Clouds and radiation processes in regional climate models evaluated using observations over the ice-free Arctic ocean. *Journal of Geophysical Research: Atmospheres* **126**(1): e2020JD033904. DOI: http://dx.doi.org/10.1029/2020JD033904.

Jakobson, E, **Vihma, T**, **Palo, T**, **Jakobson, L**, **Keernik, H**, **Jaagus, J**. 2012. Validation of atmospheric reanalyses over the central Arctic Ocean. *Geophysical Research Letters* **39**(10). DOI: http://dx.doi.org/10.1029/2012GL051591.

Jung, T, **Bauer, P**, **Goessling, H**, **Gordon, N**, **Klebe, S**, **Bromwich, D**, **Doblas-Reyes, F**, **Day, J**, **Fairall, C**, **Holland, M**, **Iversen, T**. 2015. The WWRP Polar Prediction Project (PPP), in WMO-No. 1156. Geneva, Switzerland: WMO: 371–384. (Seamless Prediction of The Earth System: From Minutes to Months).

Jung, T, **Gordon, N**, **Bauer, P**, **Bromwich, D**, **Chevallier, M**, **Day, J**, **Dawson, J**, **Doblas-Reyes, F**, **Fairall, C**, **Goessling, H**, **Holland, M**, **Inoue, J**, **Iversen, T**, **Klebe, S**, **Lemke, P**, **Losch, M**, **Makshtas, A**, **Mills, B**, **Nurmi, P**, **Perovich, D**, **Reid, P**, **Renfrew, I**, **Smith, G**, **Svensson, G**, **Tolstykh, M**, **Yang, Q**. 2016. Advancing polar prediction capabilities on daily to seasonal time scales. *Bulletin of the American Meteorological Society* **97**(9): 1631–1647. DOI: http://dx.doi.org/10.1175/BAMS-D-14-00246.1.

Knust, R. 2017. Polar research and supply vessel POLARSTERN operated by the Alfred-Wegener-Institute. *Journal of Large-Scale Research Facilities JLSRF* **3**: 119.

Lalaurette, F. 2003. Early detection of abnormal weather conditions using a probabilistic extreme forecast index. *Quarterly Journal of the Royal Meteorological Society* **129**(594): 3037–3057. DOI: http://dx.doi.org/10.1256/qj.02.152.

Messori, G, **Woods, C**, **Caballero, R**. 2018. On the drivers of wintertime temperature extremes in the high Arctic. *Journal of Climate* **31**(4): 1597–1618. DOI: http://dx.doi.org/10.1175/JCLI-D-17-0386.1.

Mortin, J, **Svensson, G**, **Graversen, RG**, **Kapsch, ML**, **Stroeve, JC**, **Boisvert, LN.** 2016. Melt onset over Arctic Sea ice controlled by atmospheric moisture transport. *Geophysical Research Letters* **43**: 6636–6642. DOI: http://dx.doi.org/10.1002/2016GL069330.

Murto, S. 2022. On the atmospheric transport pathways of heat into the Arctic in winter and spring [PhD dissertation]. Department of Meteorology, Stockholm University.

Murto, S, **Papritz, L**, **Messori, G**, **Caballero, R**, **Svensson, G**, **Wernli, H**. 2022. Extreme surface energy budget anomalies in the high Arctic in winter. *Journal of Climate* **36**(11): 3591–3609.

Naakka, T, **Nygård, T**, **Tjernström, M**, **Vihma, T**, **Pirazzini, R**, **Brooks, IM.** 2019. The impact of radiosounding observations on numerical weather prediction analyses in the Arctic. *Geophysical Research Letters* **46**(14): 8527–8535. DOI: http://dx.doi.org/10.1029/2019GL083332.

Petersen, RA. 2016. On the impact and benefits of AMDAR observations in operational forecasting–Part I: A review of the impact of automated aircraft wind and temperature reports. *Bulletin of the American Meteorological Society* **97**(4): 585–602. DOI: http://dx.doi.org/10.1175/BAMS-D-14-00055.1.

Pithan, F, **Ackerman, A**, **Angevine, WM**, **Hartung, K**, **Ickes, L**, **Kelley, M**, **Medeiros, B**, **Sandu, I**, **Steeneveld, GJ**, **Sterk, HAM**, **Svensson, G**, **Vaillancourt, PA**, **Zadra, A.** 2016. Select strengths and biases of models in representing the Arctic winter boundary layer over sea ice: The Larcform 1 single column model intercomparison. *Journal of Advances in Modeling Earth Systems* **8**(3): 1345–1357. DOI: http://dx.doi.org/10.1002/2016MS000630.

Pithan, F, **Athanase, M**, **Dahlke, S**, **Sánchez-Bentez, A**, **Shupe, MD**, **Sledd, A**, **Streffing, J**, **Svensson, G**, **Jung, T.** 2022. Nudging allows direct evaluation of coupled climate models with in-situ observations: A case study from the MOSAiC expedition. *EGUsphere* **2022**: 1–23. DOI: http://dx.doi.org/10.5194/egusphere-2022-706.

Pithan, F, **Mauritsen, T**. 2014. Arctic amplification dominated by temperature feedbacks in contemporary climate models. *Nature Geoscience* **7**(3): 181–184. DOI: http://dx.doi.org/10.1038/ngeo2071.

Pithan, F, **Svensson, G**, **Caballero, R**, **Chechin, D**, **Cronin, TW**, **Ekman, AM**, **Neggers, R**, **Shupe, MD**, **Solomon, A**, **Tjernström, M**, **Wendisch, M.** 2018. Role of air-mass transformations in exchange between the Arctic and mid-latitudes. *Nature Geoscience* **11**(11): 805–812. DOI: http://dx.doi.org/10.1038/s41561-018-0234-1.

Rantanen, M, **Karpechko, A**, **Lipponen, A**, **Nordling, K**, **Hyvärinen, O**, **Ruosteenoja, K**, **Vihma, T**, **Laaksonen, A.** 2022. The Arctic has warmed nearly four times faster than the globe since 1979. *Communications Earth & Environment* **3**(168). DOI: http://dx.doi.org/10.1038/s43247-022-00498-3.

Renfrew, IA, **Barrell, C**, **Elvidge, AD**, **Brooke, JK**, **Duscha, C**, **King, JC**, **Kristiansen, J**, **Cope, TL**, **Moore, GWK**, **Pickart, RS**, **Reuder, J**, **Sandu, I**, **Sergeev, D**, **Terpstra, A**, **Våge, K**, **Weiss, A**. 2021. An evaluation of surface meteorology and fluxes over the Iceland and Greenland Seas in ERA5 reanalysis: The impact of sea ice distribution. *Quarterly Journal of the Royal Meteorological Society* **147**(734): 691–712. DOI: http://dx.doi.org/10.1002/qj.3941.

Riihimaki, L. 2019. Radiation instruments on ice (ICERADRIIHIMAKI). 2019-10-17 to 2020-09-18 ARM Mobile Facility (MOS) collocated instruments on ice (S3). ARM Data Center. DOI: http://dx.doi.org/10.5439/1814821.

Rinke, A, **Cassano, JJ**, **Cassano, EN**, **Jaiser, R**, **Handorf, D**. 2021. Meteorological conditions during the MOSAiC expedition: Normal or anomalous? *Elementa: Science of the Anthropocene* **9**(1). DOI: http://dx.doi.org/10.1525/elementa.2021.00023.

Schwierz, C, **Croci-Maspoli, M**, **Davies, H.** 2004. Perspicacious indicators of atmospheric blocking.

Geophysical Research Letters **31**(6): L06125. DOI: http://dx.doi.org/10.1029/2003GL019341.

Shupe, M. 2022. ShupeTurner cloud microphysics product. ARM Mobile Facility (MOS) MOSAiC (Drifting Obs—Study of Arctic Climate). DOI: http://dx.doi.org/10.5439/1871015.

Shupe, MD, **Rex, M**, **Blomquist, B**, **Persson, POG**, **Schmale, J**, **Uttal, T**, **Althausen, D**, **Angot, H**, **Archer, S**, **Bariteau, L**, **Beck, I**, **Bilberry, J**, **Bucci, S**, **Buck, C**, **Boyer, M**, **Brasseur, Z**, **Brooks, IM**, **Calmer, R**, **Cassano, J**, **Castro, V**, **Chu, D**, **Costa, D**, **Cox, CJ**, **Creamean, J**, **Crewell, S**, **Dahlke, S**, **Damm, E**, **de Boer, G**, **Deckelmann, H**, **Dethloff, K**, **Dütsch, M**, **Ebell, K**, **Ehrlich, A**, **Ellis, J**, **Engelmann, R**, **Fong, AA**, **Frey, MM**, **Gallagher, MR**, **Ganzeveld, L**, **Gradinger, R**, **Graeser, J**, **Greenamyer, V**, **Griesche, H**, **Griffiths, S**, **Hamilton, J**, **Heinemann, G**, **Helmig, D**, **Herber, A**, **Heuzé, C**, **Hofer, J**, **Houchens, T**, **Howard, D**, **Inoue, J**, **Jacobi, H-W**, **Jaiser, R**, **Jokinen, T**, **Jourdan, O**, **Jozef, G**, **King, W**, **Kirchgaessner, A**, **Klingebiel, M**, **Krassovski, M**, **Krumpen, T**, **Lampert, A**, **Landing, W**, **Laurila, T**, **Lawrence, D**, **Lonardi, M**, **Loose, B**, **Lüpkes, C**, **Maahn, M**, **Macke, A**, **Maslowski, W**, **Marsay, C**, **Maturilli, M**, **Mech, M**, **Morris, S**, **Moser, M**, **Nicolaus, M**, **Ortega, P**, **Osborn, J**, **Pätzold, F**, **Perovich, DK**, **Petäjä, T**, **Pilz, C**, **Pirazzini, R**, **Posman, K**, **Powers, H**, **Pratt, KA**, **Preußer, A**, **Quéléver, L**, **Radenz, M**, **Rabe, B**, **Rinke, A**, **Sachs, T**, **Schulz, A**, **Siebert, H**, **Silva, T**, **Solomon, A**, **Sommerfeld, A**, **Spreen, G**, **Stephens, M**, **Stohl, A**, **Svensson, G**, **Uin, J**, **Viegas, J**, **Voigt, C**, **von der Gathen, P**, **Wehner, P**, **Welker, JM**, **Wendisch, M**, **Werner, M**, **Xie, Z**, **Yue, F**. 2022. Overview of the MOSAiC expedition: Atmosphere. *Elementa: Science of the Anthropocene* **10**(1). DOI: http://dx.doi.org/10.1525/elementa.2021.00060.

Shupe, MD, **Turner, DD**, **Zwink, A**, **Thieman, MM**, **Mlawer, EJ**, **Shippert, T.** 2015. Deriving Arctic cloud microphysics at Barrow, Alaska: Algorithms, results, and radiative closure. *Journal of Applied Meteorology and Climatology* **54**(7): 1675–1689. DOI: http://dx.doi.org/10.1175/JAMC-D-15-0054.1.

Solomon, A, **Shupe, MD**, **Svensson, G**, **Barton, N**, **Batrak, Y**, **Bazile, E**, **Day, JJ**, **Doyle, JD**, **Frank, HP**, **Keeley, S**, **Remes, T**, **Tolstykh, M**. 2023. The winter central Arctic surface energy budget: A model evaluation using observations from the MOSAiC campaign. *Elementa: Science of the Anthropocene* **11**(1): 00104. DOI: https://doi.org/10.1525/elementa.2022.00104.

Sprenger, M, **Wernli, H.** 2015. The LAGRANTO Lagrangian analysis tool–version 2.0. *Geoscientific Model Development* **8**(8): 2569–2586. DOI: http://dx.doi.org/10.5194/gmd-8-2569-2015.

Svensson, G, **Karlsson, J.** 2011. On the Arctic wintertime climate in global climate models. *Journal of Climate* **24**(22): 5757–5771. DOI: http://dx.doi.org/10.1175/2011JCLI4012.1.

Tjernström, M, **Leck, C**, **Birch, CE**, **Bottenheim, JW**, **Brooks, BJ**, **Brooks, IM**, **Bäcklin, L**, **Chang, RY-W**, **de Leeuw, G**, **Di Liberto, L**, **de la Rosa, S**, **Granath, E**, **Graus, M**, **Hansel, A**, **Heintzenberg, J**, **Held, A**, **Hind, A**, **Johnston, P**, **Knulst, J**, **Martin, M**, **Matrai, PA**, **Mauritsen, T**, **Müller, M**, **Norris, SJ**, **Orellana, MV**, **Orsini, DA**, **Paatero, J**, **Persson, POG**, **Gao, Q**, **Rauschenberg, C**, **Ristovski, Z**, **Sedlar, J**, **Shupe, MD**, **Sierau, B**, **Sirevaag, A**, **Sjogren, S**, **Stetzer, O**, **Swietlicki, E**, **Szczodrak, M**, **Vaattovaara, P**, **Wahlberg, N**, **Westberg, M**, **Wheeler, CR**. 2014. The Arctic Summer Cloud Ocean Study (ASCOS): Overview and experimental design. *Atmospheric Chemistry and Physics* **14**(6): 2823–2869. DOI: http://dx.doi.org/10.5194/acp-14-2823-2014.

Tjernström, M, **Svensson, G**, **Magnusson, L**, **Brooks, IM**, **Prytherch, J**, **Vüllers, J**, **Young, G.** 2021. Central Arctic weather forecasting: Confronting the ECMWF IFS with observations from the Arctic Ocean 2018 expedition. *Quarterly Journal of the Royal Meteorological Society* **147**(735): 1278–1299.

Vihma, T, **Uotila, J**, **Cheng, B**, **Launiainen, J**. 2002. Surface heat budget over the Weddell Sea: Buoy results and model comparisons. *Journal of Geophysical Research: Oceans* **107**(C2): 5–1–5–15. DOI: http://dx.doi.org/10.1029/2000JC000372.

Woods, C, **Caballero, R**, **Svensson, G.** 2013. Large-scale circulation associated with moisture intrusions into the Arctic during winter. *Geophysical Research Letters* **40**(17): 4717–4721. DOI: http://dx.doi.org/10.1002/grl.50912.

How to cite this article: Svensson, G, Murto, S, Shupe, MD, Pithan, F, Magnusson, L, Day, JJ, Doyle, JD, Renfrew, IA, Spengler, T, Vihma, T. 2023. Warm air intrusions reaching the MOSAiC expedition in April 2020—The YOPP targeted observing period (TOP). *Elementa: Science of the Anthropocene* 11(1). DOI: https://doi.org/10.1525/elementa.2023.00016

Domain Editor-in-Chief: Detlev Helmig, Boulder AIR LLC, Boulder, CO, USA

Associate Editor: Joël Savarino, Laboratoire de Glaciologie et Géophysique de l'Environnement, CNRS/Grenoble University, Saint-Martin d'Hères, France

Knowledge Domain: Atmospheric Science

Part of an Elementa Special Feature: The Multidisciplinary Drifting Observatory for the Study of Arctic Climate (MOSAiC)

Published: June 28, 2023 **Accepted:** April 18, 2023 **Submitted:** January 5, 2023

ELEMENTA
Science of the Anthropocene

Elem Sci Anth is a peer-reviewed open access
journal published by University of California Press.

OPEN ACCESS